Available online at www.sciencedirect.com
ScienceDirect
Journal of Sound and Vibration 305 (2007) 401–431
JOURNAL OF SOUND AND VIBRATION
www.elsevier.com/locate/jsvi

A numerical model for calculating vibration from a railway tunnel embedded in a full-space

M.F.M. Hussein[a,*], H.E.M. Hunt[b]

[a]School of Civil Engineering, University of Nottingham, University Park, Nottingham, NG7 2RD, UK
[b]Engineering Department, Cambridge University, Trumpington Street, Cambridge, CB2 1PZ, UK

Received 30 October 2006; received in revised form 12 March 2007; accepted 28 March 2007
Available online 15 June 2007

Abstract

Vibration generated by underground railways transmits to nearby buildings causing annoyance to inhabitants and malfunctioning to sensitive equipment. Vibration can be isolated through countermeasures by reducing the stiffness of railpads, using floating-slab tracks and/or supporting buildings on springs. Modelling of vibration from underground railways has recently gained more importance on account of the need to evaluate accurately the performance of vibration countermeasures before these are implemented.

This paper develops an existing model, reported by Forrest and Hunt, for calculating vibration from underground railways. The model, known as the Pipe-in-Pipe model, has been developed in this paper to account for anti-symmetrical inputs and therefore to model tangential forces at the tunnel wall. Moreover, three different arrangements of supports are considered for floating-slab tracks, one which can be used to model directly-fixed slabs. The paper also investigates the wave-guided solution of the track, the tunnel, the surrounding soil and the coupled system. It is shown that the dynamics of the track have significant effect on the results calculated in the wavenumber–frequency domain and therefore an important role on controlling vibration from underground railways.
© 2007 Elsevier Ltd. All rights reserved.

1. Introduction

Researches on vibration from underground railways have gained a special interest in the last few decades. The general trend towards lighter constructions with longer spans along with the introduction of new underground railway lines in urban areas, have led to more vibration in buildings. This in turn has led to more complaints from occupants of buildings. There are many methods to decrease ground-borne vibration in buildings. They generally fall into three categories. Vibration isolation can be achieved by isolating the source, interrupting the vibration path and/or isolating the receiver, i.e. the building. Floating-slab tracks, open and in-filled trenches and base isolation of buildings are typical examples of the three categories, respectively. The right choice of vibration countermeasure and its specification is crucial because of the high financial cost and the difficulty of retrospective replacement. Modelling of vibration from underground railways has become

*Corresponding author. Tel.: +44 1159 513904; fax: +44 1159 513898.
E-mail addresses: mohammed.hussein@nottingham.ac.uk (M.F.M. Hussein), hemh1@cam.ac.uk (H.E.M. Hunt).

0022-460X/$ - see front matter © 2007 Elsevier Ltd. All rights reserved.
doi:10.1016/j.jsv.2007.03.068

more important with more concerns about the expected performance of vibration countermeasures. In this section, some of the relevant literature on modelling of vibration from underground railways is reviewed.

Lai et al. [1] develops a technique to predict vibration in buildings from an underground tunnel in the city of Rome. The technique is based on a combination of numerical modelling and field measurements. The railway track was not constructed at the time of the study which was conducted to compare the expected perceived vibration with the permissible vibration levels in buildings according to the ISO standards. The technique is divided into three different parts to account for the source, i.e. the train and the track system; the transmission path, i.e. the tunnel, medium and building; and the receiver, i.e. a human individual.

Sheng et al. [2] present a numerical method based on the discrete wavenumber fictitious force method to model an underground tunnel embedded in a half-space. The method depends on writing the boundary integral equations of only the displacement Green's function. This is an advantage over the Boundary Element (BE) method as the traction Green's function is not required.

The coupled Finite Element–Boundary Element (FE–BE) technique is frequently used to model vibration from underground railways. The FE method is used to model a tunnel wall while the BE method is used to model the surrounding single or multi-layered ground.

Sheng et al. [3] describe a numerical model based on the coupled FE–BE technique. The computational efficiency is improved by incorporating the discrete wavenumber method. The method takes advantage of that the track and its surrounding ground are invariant in the track direction and therefore reduces the modelling effort to a single vertical transverse problem, also known as a two-and-half-dimensional problem.

Clouteau et al. [4] present an efficient numerical model based on the coupled FE–BE method for calculating vibration from underground railways. The technique incorporates the Floquet transformation that accounts for periodicity in the tunnel direction, which significantly improves the computational efficiency. The technique has an advantage over the two-and-a-half-dimensional approaches as the periodic Green's kernel incorporated has the same singularities as the three-dimensional (3D) Green's kernel. The model is used to calculate vibration from a shallow cut-and-cover masonry tunnel in Paris [4,5] and from a deep bored tunnel of London Underground [5].

Andersen and Jones [6,7] use a coupled FE and BE analysis to compare between 2D and 3D modelling. An important finding of their work is that 2D modelling can give only qualitative results. However, it provides a quick tool to assess vibration isolation measures.

The Finite Difference (FD) method [8] can also be used to model vibration from underground railways. The advantage of this method is that less effort is needed to write the code compared with other conventional methods, however on the expense of reducing the computational efficiency.

A computationally efficient model for calculating vibration from underground railways is presented by Forrest and Hunt [9,10]. The model is known as the Pipe-in-Pipe (PiP) where a tunnel wall and its surrounding infinite soil are modelled as two concentric pipes. The inner pipe represents the tunnel wall and is modelled using the thin shell theory. The outer pipe, with its outer radius being set to infinity, represents an infinite soil with a cylindrical cavity and is modelled using the elastic continuum theory. The PiP model is computationally efficient on account of the uniformity along and around the tunnel.

The PiP model has been recently validated against the coupled FE–BE model for the case of a tunnel embedded within a full-space [11]. A good agreement is achieved between results of the two models.

Hussein and Hunt [12] have developed the PiP model into a software with a user-friendly interface. The software is available on the internet as a freeware [13] that accounts for a train running on a floating-slab track in the tunnel. The software calculates the power spectral density (PSD) of the vertical displacement at any selected point in the soil for a roughness excitation of a unit value (i.e. white noise). The software also calculates the insertion gain (IG), which is the ratio between the PSD displacement before and after changing parameters of the track, tunnel or soil. The latest version of the software plots the displacement contours around the tunnel and accounts for a bedrock layer below the tunnel using the mirror-image method [12,13].

The study presented in this paper is used in Ref. [14], where a new method is presented for evaluating vibration countermeasures in underground tunnels. It should be noted that the PiP model as reported by Forrest and Hunt does not account for a free surface. A computationally efficient model that is based on the PiP model and accounts for a free surface is presented in Ref. [15].

Another model for calculating vibration from underground railways is presented by Grundmann and Muller [16]. The model accounts for circular and non-circular tunnels in a full-space and a half-space. To account for a circular tunnel in a full-space, the shell theory or the FE method is used for the tunnel and the elastic continuum theory is used for the soil. To account for a non-circular tunnel in a full-space, the model is divided into two parts by a virtual cylindrical surface that encloses the tunnel wall. The first is the internal part and it consists of the tunnel wall and soil that lies within the virtual cylinder. This part is modelled using the FE method. The second part is the homogeneous infinite space with an internal cylindrical boundary and this is modelled using the elastic continuum theory. A half-space is modelled by using superposition of two boundary value problems [17,18]. These are: (1) a tunnel embedded in a full-space and (2) an elastic half-space.

The current paper builds on the work of Forrest and Hunt [9,10]. There are three main features of the new work. The first is that the displacements of the PiP model are calculated for anti-symmetrical inputs on the tunnel wall. This allows calculation of the response of the PiP model for tangential forces applied on the tunnel wall. Note that in the work of Forrest and Hunt, the displacements of the PiP model are calculated for symmetrical loads (about one of the tunnel axis-of-symmetry in the cross-sectional plane) and therefore tangential inputs to the tunnel are not modelled. The second feature is that three different arrangements of slab bearings are considered. The track is coupled to the PiP model via two lines, three lines and uniform support. This is done to identify a way of controlling vibration from underground railways by changing the slab connectivity. The uniform support is used to model the direct fixation case by setting the stiffness of slab bearings to infinity. In reality, a floating slab is mounted on a thick layer of concrete in the base of the tunnel. Such a layer can be modelled as an extra directly-fixed slab as demonstrated below. The inclusion of this layer is currently under development by the authors. The third feature is that dispersion curves of the PiP model and the track model are investigated. This provides a better understanding of the vibration results for harmonic loads applied on the rails.

This paper falls into five sections. Section 2 presents the model and provides the necessary equations to calculate displacements of the track for different types of support distribution, i.e. slab-bearings distribution. Section 3 shows the calculation of Frequency Response Functions (FRFs), including those for the PiP model. Section 4 demonstrates the method used to express the stiffness of slab bearings. Section 5 investigates the dispersion characteristics of the model and discusses the displacement results of the soil due to any input loads on the rails.

2. Formulation of the model

Three distribution of supports, i.e. slab bearings are considered in this section. Floating slabs are coupled to the tunnel via two lines, three lines or uniform support resulting in three different models. These models are shown in Fig. 1(a–c) and are analysed in the following three sections, respectively. Note that the soil is considered in the formulation but not shown in the figure. The slab is modelled in both bending and torsion. The purpose of the analysis is to calculate the displacements of the rails, slab and PiP model in the wavenumber–frequency domain. The reader with little knowledge about coupling in the wavenumber–frequency domain is referred to Appendix A in Ref. [19] where the method is illustrated.

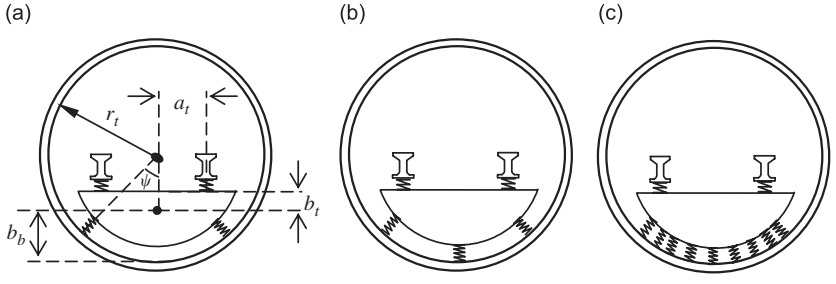

Fig. 1. Floating-slab tracks attached to the tunnel wall via: (a) two lines of support, (b) three lines of support and (c) uniform layer. Railpads and slab bearings are continuous along the tunnel.

2.1. Track with two lines of support

Fig. 2a shows the model, where all forces are in the form $F = \tilde{F}e^{i(\omega t+\xi x)}$ and all displacements are in the form $y = \tilde{y}e^{i(\omega t+\xi x)}$. Two forces are applied on the left and the right rails denoted F_1 and F_2, respectively. The rails are assumed to vibrate only in the vertical direction as described by y_1 and y_2. The vertical, horizontal and rotational displacements of the slab are described by y_3, y_4 and y_5, respectively.

Fig. 2b shows the forces and displacements on the free body diagrams of the rails and the slab. Fig. 2c shows the forces on the left railpads and the left support. The tunnel displacements at the contact points with the slab bearings are shown in Fig. 2d. The model has nine degrees of freedom and the input forces are only allowed at two degrees of freedom, i.e. on the rails. For given values of $\tilde{F}_1$ and $\tilde{F}_2$, the displacements and induced forces are calculated by writing the equilibrium and compatibility equations in the wavenumber–frequency domain. Equations of equilibrium of the left and right rails read

$$\tilde{y}_1 = \tilde{H}_r(\tilde{F}_1 - \tilde{G}_{r1}) \tag{1}$$

and

$$\tilde{y}_2 = \tilde{H}_r(\tilde{F}_2 - \tilde{G}_{r2}), \tag{2}$$

where $\tilde{H}_r$ is the FRF of one of the rails in the vertical direction, as the two rails are identical, $\tilde{G}_{r1}$ and $\tilde{G}_{r2}$ are the forces transmitted to the slab from the left and the right rails, respectively. The equations of equilibrium of the slab in the vertical, horizontal and rotational directions are:

$$\tilde{y}_3 = \tilde{H}_v(-\tilde{P}_1\cos\psi - \tilde{P}_2\cos\psi + \tilde{Q}_1\sin\psi - \tilde{Q}_2\sin\psi + \tilde{G}_{r1} + \tilde{G}_{r2}), \tag{3}$$

$$\tilde{y}_4 = \tilde{H}_h(-\tilde{P}_1\sin\psi + \tilde{P}_2\sin\psi - \tilde{Q}_1\cos\psi - \tilde{Q}_2\cos\psi) \tag{4}$$

and

$$\tilde{y}_5 = \tilde{H}_\gamma\{(\tilde{G}_{r1} - \tilde{G}_{r2})a_t - (\tilde{Q}_1 + \tilde{Q}_2)[r_t - (r_t - b_b)\cos\psi] + (\tilde{P}_1 - \tilde{P}_2)(r_t - b_b)\sin\psi\}, \tag{5}$$

where $\tilde{H}_v$, $\tilde{H}_h$ and $\tilde{H}_\gamma$ are the FRFs of the slab in the vertical, horizontal and rotational directions, respectively, and their calculations will be shown later, ψ is the central angle of the bearings (see Fig. 1a), r_t the inner radius of the tunnel, a_t the horizontal distance between the slab centre and either the left or the right rail and b_b the vertical distance between the slab centre and the bottom of the slab. Note that this is equivalent to the distance between the slab centre and the tunnel invert as the bearing's height is relatively small.

The equilibrium equations of the railpads are given by

$$\tilde{G}_{r1} = k_r\tilde{y}_1 - k_r\tilde{y}_3 - k_r a_t\tilde{y}_5 \tag{6}$$

and

$$\tilde{G}_{r2} = k_r\tilde{y}_2 - k_r\tilde{y}_3 + k_r a_t\tilde{y}_5, \tag{7}$$

where k_r is the normal stiffness of the railpads.

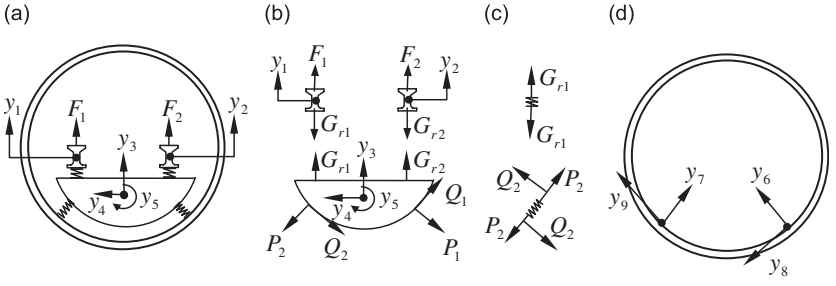

Fig. 2. Modelling a track on two lines of support: (a) external forces on the rails and degrees of freedom of the track, (b) free-body diagrams of the rails and the slab, (c) forces on the left railpad and left slab bearings and (d) the tunnel wall displacements at the interface.

The equilibrium equations of the slab bearings are given by

$$\tilde{P}_1 = k_n[\tilde{y}_3 \cos\psi + \tilde{y}_4 \sin\psi - \tilde{y}_5(r_t - b_b)\sin\psi - \tilde{y}_6], \tag{8}$$

$$\tilde{P}_2 = k_n[\tilde{y}_3 \cos\psi - \tilde{y}_4 \sin\psi + \tilde{y}_5(r_t - b_b)\sin\psi - \tilde{y}_7], \tag{9}$$

$$\tilde{Q}_1 = k_s\{-\tilde{y}_3 \sin\psi + \tilde{y}_4 \cos\psi + \tilde{y}_5[r_t - (r_t - b_b)\cos\psi] - \tilde{y}_8\} \tag{10}$$

and

$$\tilde{Q}_2 = k_s\{\tilde{y}_3 \sin\psi + \tilde{y}_4 \cos\psi + \tilde{y}_5[r_t - (r_t - b_b)\cos\psi] - \tilde{y}_9\}, \tag{11}$$

where k_n and k_s are the normal and shear stiffness, respectively, of the slab bearings.

The equilibrium equations at the inner surface of the tunnel for the PiP model are:

$$\tilde{y}_6 = \tilde{H}_{6-6}\tilde{P}_1 + \tilde{H}_{6-7}\tilde{P}_2 + \tilde{H}_{6-8}\tilde{Q}_1 + \tilde{H}_{6-9}\tilde{Q}_2, \tag{12}$$

$$\tilde{y}_7 = \tilde{H}_{7-6}\tilde{P}_1 + \tilde{H}_{7-7}\tilde{P}_2 + \tilde{H}_{7-8}\tilde{Q}_1 + \tilde{H}_{7-9}\tilde{Q}_2, \tag{13}$$

$$\tilde{y}_8 = \tilde{H}_{8-6}\tilde{P}_1 + \tilde{H}_{8-7}\tilde{P}_2 + \tilde{H}_{8-8}\tilde{Q}_1 + \tilde{H}_{8-9}\tilde{Q}_2 \tag{14}$$

and

$$\tilde{y}_9 = \tilde{H}_{9-6}\tilde{P}_1 + \tilde{H}_{9-7}\tilde{P}_2 + \tilde{H}_{9-8}\tilde{Q}_1 + \tilde{H}_{9-9}\tilde{Q}_2, \tag{15}$$

where $\tilde{H}_{j-k}$ is the FRF of the PiP model, which expresses the displacement of the jth degree of freedom for a unit input applied on the kth degree of freedom in the wavenumber–frequency domain. Calculations of these values will be shown in Section 3.

To solve Eqs. (1)–(15), they are rewritten in matrix form as follows:

$$\tilde{\mathbf{y}}_\mathbf{R} = \tilde{\mathbf{H}}_{11}\tilde{\mathbf{G}}_\mathbf{R} + \tilde{\mathbf{H}}_{12}\tilde{\mathbf{F}}_\mathbf{R}, \tag{16}$$

$$\tilde{\mathbf{y}}_\mathbf{S} = \tilde{\mathbf{H}}_{21}\tilde{\mathbf{P}} + \tilde{\mathbf{H}}_{22}\tilde{\mathbf{G}}_\mathbf{R}, \tag{17}$$

$$\tilde{\mathbf{G}}_\mathbf{R} = \tilde{\mathbf{H}}_{31}\tilde{\mathbf{y}}_\mathbf{R} + \tilde{\mathbf{H}}_{32}\tilde{\mathbf{y}}_\mathbf{S}, \tag{18}$$

$$\tilde{\mathbf{P}} = \tilde{\mathbf{H}}_{41}\tilde{\mathbf{y}}_\mathbf{S} + \tilde{\mathbf{H}}_{42}\tilde{\mathbf{y}}_\mathbf{T} \tag{19}$$

and

$$\tilde{\mathbf{y}}_\mathbf{T} = \tilde{\mathbf{H}}_{51}\tilde{\mathbf{P}}, \tag{20}$$

where

$$\tilde{\mathbf{y}}_\mathbf{R} = [\tilde{y}_1, \tilde{y}_2]^\mathrm{T}, \quad \tilde{\mathbf{G}}_\mathbf{R} = [\tilde{G}_{r1}, \tilde{G}_{r2}]^\mathrm{T}, \quad \tilde{\mathbf{F}}_\mathbf{R} = [\tilde{F}_1, \tilde{F}_2]^\mathrm{T}, \quad \tilde{\mathbf{y}}_\mathbf{S} = [\tilde{y}_3, \tilde{y}_4, \tilde{y}_5]^\mathrm{T},$$

$$\tilde{\mathbf{P}} = [\tilde{P}_1, \tilde{P}_2, \tilde{Q}_1, \tilde{Q}_2]^\mathrm{T}, \quad \tilde{\mathbf{y}}_\mathbf{T} = [\tilde{y}_6, \tilde{y}_7, \tilde{y}_8, \tilde{y}_9]^\mathrm{T}, \quad \tilde{\mathbf{H}}_{11} = \begin{bmatrix} -\tilde{H}_r & 0 \\ 0 & -\tilde{H}_r \end{bmatrix},$$

$$\tilde{\mathbf{H}}_{21} = \begin{bmatrix} \tilde{H}_r & 0 \\ 0 & \tilde{H}_r \end{bmatrix},$$

$$\tilde{\mathbf{H}}_{21} = \begin{bmatrix} -\tilde{H}_v\cos\psi & -\tilde{H}_v\cos\psi & \tilde{H}_v\sin\psi & -\tilde{H}_v\sin\psi \\ -\tilde{H}_h\sin\psi & \tilde{H}_h\sin\psi & -\tilde{H}_h\cos\psi & -\tilde{H}_h\cos\psi \\ \tilde{H}_\gamma(r_t - b_b)\sin\psi & -\tilde{H}_\gamma(r_t - b_b)\sin\psi & -\tilde{H}_\gamma[r_t - (r_t - b_b)\cos\psi] & -\tilde{H}_\gamma[r_t - (r_t - b_b)\cos\psi] \end{bmatrix},$$

$$\tilde{\mathbf{H}}_{22}=\begin{bmatrix}\tilde{H}_v & \tilde{H}_v\\ 0 & 0\\ \tilde{H}_\gamma a_t & -\tilde{H}_\gamma a_t\end{bmatrix},\quad \tilde{\mathbf{H}}_{31}=\begin{bmatrix}k_r & 0\\ 0 & k_r\end{bmatrix},\quad \tilde{\mathbf{H}}_{32}=\begin{bmatrix}-k_r & 0 & -k_r a_t\\ -k_r & 0 & k_r a_t\end{bmatrix},$$

$$\tilde{\mathbf{H}}_{41}=\begin{bmatrix}k_n\cos\psi & k_n\sin\psi & -k_n(r_t-b_b)\sin\psi\\ k_n\cos\psi & -k_n\sin\psi & k_n(r_t-b_b)\sin\psi\\ -k_s\sin\psi & k_s\cos\psi & k_s[r_t-(r_t-b_b)\cos\psi]\\ k_s\sin\psi & k_s\cos\psi & k_s[r_t-(r_t-b_b)\cos\psi]\end{bmatrix},$$

$$\tilde{\mathbf{H}}_{42}=\begin{bmatrix}-k_n & 0 & 0 & 0\\ 0 & -k_n & 0 & 0\\ 0 & 0 & -k_s & 0\\ 0 & 0 & 0 & -k_s\end{bmatrix}$$

and

$$\tilde{\mathbf{H}}_{51}=\begin{bmatrix}\tilde{H}_{6-6} & \tilde{H}_{6-7} & \tilde{H}_{6-8} & \tilde{H}_{6-9}\\ \tilde{H}_{7-6} & \tilde{H}_{7-7} & \tilde{H}_{7-8} & \tilde{H}_{7-9}\\ \tilde{H}_{8-6} & \tilde{H}_{8-7} & \tilde{H}_{8-8} & \tilde{H}_{8-9}\\ \tilde{H}_{9-6} & \tilde{H}_{9-7} & \tilde{H}_{9-8} & \tilde{H}_{9-9}\end{bmatrix}.$$

Solving Eqs. (19) and (20) for $\tilde{\mathbf{P}}$:

$$\tilde{\mathbf{P}}=(\mathbf{I}_4-\tilde{\mathbf{H}}_{42}\tilde{\mathbf{H}}_{51})^{-1}\tilde{\mathbf{H}}_{41}\tilde{\mathbf{y}}_{\mathbf{s}},\tag{21}$$

where $\mathbf{I}_n$ is the identity matrix of size $n\times n$. Solving Eqs. (16) and (18) for $\tilde{\mathbf{G}}_{\mathbf{R}}$:

$$\tilde{\mathbf{G}}_{\mathbf{R}}=(\mathbf{I}_2-\tilde{\mathbf{H}}_{31}\tilde{\mathbf{H}}_{11})^{-1}(\tilde{\mathbf{H}}_{31}\tilde{\mathbf{H}}_{12}\tilde{\mathbf{F}}_{\mathbf{R}}+\tilde{\mathbf{H}}_{32}\tilde{\mathbf{y}}_{\mathbf{s}}).\tag{22}$$

Solving Eqs. (22) and (17) for $\tilde{\mathbf{y}}_{\mathbf{s}}$ and substituting $\tilde{\mathbf{P}}$ from Eq. (21):

$$\tilde{\mathbf{y}}_{\mathbf{s}}=[\mathbf{I}_3-\tilde{\mathbf{H}}_{22}(\mathbf{I}_2-\tilde{\mathbf{H}}_{31}\tilde{\mathbf{H}}_{11})^{-1}\tilde{\mathbf{H}}_{32}-\tilde{\mathbf{H}}_{21}(\mathbf{I}_4-\tilde{\mathbf{H}}_{42}\tilde{\mathbf{H}}_{51})^{-1}\tilde{\mathbf{H}}_{41}]^{-1}\tilde{\mathbf{H}}_{22}(\mathbf{I}_2-\tilde{\mathbf{H}}_{31}\tilde{\mathbf{H}}_{11})^{-1}\tilde{\mathbf{H}}_{31}\tilde{\mathbf{H}}_{12}\tilde{\mathbf{F}}_{\mathbf{R}}.\tag{23}$$

Eqs. (23), (21) and (20) form the necessary equations to calculate $\tilde{\mathbf{y}}_{\mathbf{s}}$, $\tilde{\mathbf{P}}$ and $\tilde{\mathbf{y}}_{\mathbf{T}}$, respectively.

2.2. Track with three lines of support

This model has two more degrees of freedom compared with the previous one. These are the radial and shear displacement of the PiP model at the tunnel invert. The model is shown in Fig. 3, with three lines of support. The side slab bearings lie at a central angle ψ with the tunnel invert. The procedure followed in Section 2.1 is applied here to calculate the displacements for this model. The equivalent set of equations

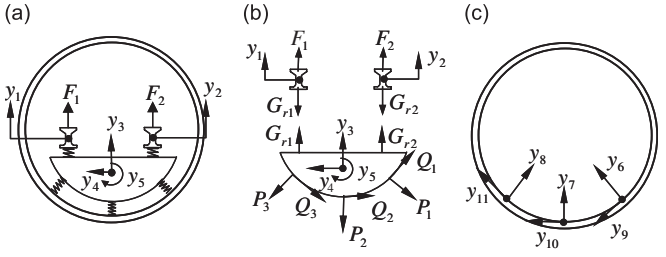

Fig. 3. Modelling a track on three lines of support: (a) external forces on the rails and degrees of freedom of the track, (b) free-body diagrams of the rails and the slab and (c) the tunnel wall displacements at the interface.

corresponding to Eqs. (23), (21) and (20) are:

$$\tilde{\mathbf{y}}_{\mathbf{s}} = [\mathbf{I}_3 - \tilde{\mathbf{H}}_{22}(\mathbf{I}_2 - \tilde{\mathbf{H}}_{31}\tilde{\mathbf{H}}_{11})^{-1}\tilde{\mathbf{H}}_{32} - \tilde{\mathbf{H}}_{21}(\mathbf{I}_6 - \tilde{\mathbf{H}}_{42}\tilde{\mathbf{H}}_{51})^{-1}\tilde{\mathbf{H}}_{41}]^{-1}\tilde{\mathbf{H}}_{22}(\mathbf{I}_2 - \tilde{\mathbf{H}}_{31}\tilde{\mathbf{H}}_{11})^{-1}\tilde{\mathbf{H}}_{31}\tilde{\mathbf{H}}_{12}\tilde{\mathbf{F}}_{\mathbf{R}}, \tag{24}$$

$$\tilde{\mathbf{P}} = (\mathbf{I}_6 - \tilde{\mathbf{H}}_{42}\tilde{\mathbf{H}}_{51})^{-1}\tilde{\mathbf{H}}_{41}\tilde{\mathbf{y}}_{\mathbf{s}} \tag{25}$$

and

$$\tilde{\mathbf{y}}_{\mathbf{T}} = \tilde{\mathbf{H}}_{51}\tilde{\mathbf{P}}, \tag{26}$$

where

$$\tilde{\mathbf{H}}_{21} = \begin{bmatrix} -\tilde{H}_v\cos\psi & -\tilde{H}_v & -\tilde{H}_v\cos\psi & \tilde{H}_v\sin\psi & 0 & -\tilde{H}_v\sin\psi \\ -\tilde{H}_h\sin\psi & 0 & \tilde{H}_h\sin\psi & -\tilde{H}_h\cos\psi & -\tilde{H}_h & -\tilde{H}_h\cos\psi \\ \tilde{H}_\gamma(r_t-b_b)\sin\psi & 0 & -\tilde{H}_\gamma(r_t-b_b)\sin\psi & -\tilde{H}_\gamma[r_t-(r_t-b_b)\cos\psi] & -\tilde{H}_\gamma b_b & -\tilde{H}_\gamma[r_t-(r_t-b_b)\cos\psi] \end{bmatrix},$$

$$\tilde{\mathbf{H}}_{41} = \begin{bmatrix} k_n\cos\psi & k_n\sin\psi & -k_n(r_t-b_b)\sin\psi \\ k_n & 0 & 0 \\ k_n\cos\psi & -k_n\sin\psi & k_n(r_t-b_b)\sin\psi \\ -k_s\sin\psi & k_s\cos\psi & k_s[r_t-(r_t-b_b)\cos\psi] \\ 0 & k_s & k_s b_b \\ k_s\sin\psi & k_s\cos\psi & k_n[r_t-(r_t-b_b)\cos\psi] \end{bmatrix},$$

$$\tilde{\mathbf{H}}_{42} = \begin{bmatrix} -k_n & 0 & 0 & 0 & 0 & 0 \\ 0 & -k_n & 0 & 0 & 0 & 0 \\ 0 & 0 & -k_n & 0 & 0 & 0 \\ 0 & 0 & 0 & -k_s & 0 & 0 \\ 0 & 0 & 0 & 0 & -k_s & 0 \\ 0 & 0 & 0 & 0 & 0 & -k_s \end{bmatrix}$$

and

$$\tilde{\mathbf{H}}_{51} = \begin{bmatrix} \tilde{H}_{6-6} & \tilde{H}_{6-7} & \tilde{H}_{6-8} & \tilde{H}_{6-9} & \tilde{H}_{6-10} & \tilde{H}_{6-11} \\ \tilde{H}_{7-6} & \tilde{H}_{7-7} & \tilde{H}_{7-8} & \tilde{H}_{7-9} & \tilde{H}_{7-10} & \tilde{H}_{7-11} \\ \tilde{H}_{8-6} & \tilde{H}_{8-7} & \tilde{H}_{8-8} & \tilde{H}_{8-9} & \tilde{H}_{8-10} & \tilde{H}_{8-11} \\ \tilde{H}_{9-6} & \tilde{H}_{9-7} & \tilde{H}_{9-8} & \tilde{H}_{9-9} & \tilde{H}_{9-10} & \tilde{H}_{9-11} \\ \tilde{H}_{10-6} & \tilde{H}_{10-7} & \tilde{H}_{10-8} & \tilde{H}_{10-9} & \tilde{H}_{10-10} & \tilde{H}_{10-11} \\ \tilde{H}_{11-6} & \tilde{H}_{11-7} & \tilde{H}_{11-8} & \tilde{H}_{11-9} & \tilde{H}_{11-10} & \tilde{H}_{11-11} \end{bmatrix}.$$

All the other matrices and vectors in Eqs. (24)–(26), are same as defined in Section 2.1.

2.3. Track with uniform support

The floating slab in this case is connected to the PiP model via a uniform support as shown in Fig. 4 with a central angle ψ between the tunnel invert and the bearings end. The normal and shear stiffness of the bearings have units of N/m/m^2 rather than N/m/m as in the previous sections. Displacements of the track and the PiP model are calculated by writing the equilibrium equations in the wavenumber–frequency domain.

The equilibrium equations of the rails are identical to Eqs. (1) and (2). The equilibrium equations of the slab are written as

$$\tilde{y}_3 = \tilde{H}_v\left(\tilde{G}_{r1} + \tilde{G}_{r2} - \int_{-\psi}^{\psi}\tilde{P}_\theta\cos\theta\, r_t\,\mathrm{d}\theta - \int_{-\psi}^{\psi}\tilde{Q}_\theta\sin\theta\, r_t\,\mathrm{d}\theta\right), \tag{27}$$

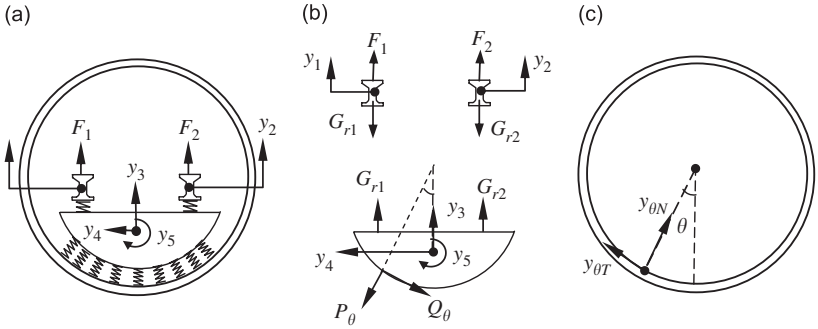

Fig. 4. Modelling a track on a uniform support: (a) external forces on the rails and degrees of freedom of the track, (b) free-body diagrams of the rails and the slab and (c) the tunnel wall displacement at angle θ at the interface.

$$\tilde{y}_4 = \tilde{H}_h\left(\int_{-\psi}^{\psi} \tilde{P}_\theta \sin\theta\, r_t\, \mathrm{d}\theta - \int_{-\psi}^{\psi} \tilde{Q}_\theta \cos\theta\, r_t\, \mathrm{d}\theta\right) \tag{28}$$

and

$$\tilde{y}_5 = \tilde{H}_\gamma\left\{[\tilde{G}_{r1} - \tilde{G}_{r2}]\, a_t - \int_{-\psi}^{\psi} \tilde{P}_\theta (r_t - b_b)\sin\theta\, r_t\, \mathrm{d}\theta - \int_{-\psi}^{\psi} \tilde{Q}_\theta [r_t - (r_t - b_b)\cos\theta] r_t\, \mathrm{d}\theta\right\}, \tag{29}$$

where $\tilde{P}_\theta$ and $\tilde{Q}_\theta$ are the induced forces for the PiP model on the tunnel wall at a central angle θ as shown in Fig. 4b. The equilibrium equations for the railpads are identical to Eqs. (6) and (7). The equilibrium equations for slab bearings at angle θ are written as

$$\tilde{P}_\theta = k_n[\tilde{y}_3 \cos\theta - \tilde{y}_4 \sin\theta + \tilde{y}_5(r_t - b_b)\sin\theta - \tilde{y}_{\theta N}] \tag{30}$$

and

$$\tilde{Q}_\theta = k_s\{\tilde{y}_3 \sin\theta + \tilde{y}_4 \cos\theta + \tilde{y}_5[r_t - (r_t - b_b)\cos\theta] - \tilde{y}_{\theta T}], \tag{31}$$

where $\tilde{y}_{\theta N}$ and $\tilde{y}_{\theta T}$ are the displacements of the tunnel wall at a central angle θ as shown in Fig. 4c. The equilibrium equations of the PiP model are written as follows:

$$\tilde{y}_{\theta N} = \left(\int_{-\psi}^{\psi} \tilde{P}_\tau \tilde{H}_{\theta\tau}^{NN}\, r_t\, \mathrm{d}\tau + \int_{-\psi}^{\psi} \tilde{Q}_\tau \tilde{H}_{\theta\tau}^{NT}\, r_t\, \mathrm{d}\tau\right) \tag{32}$$

and

$$\tilde{y}_{\theta T} = \left(\int_{-\psi}^{\psi} \tilde{P}_\tau \tilde{H}_{\theta\tau}^{TN}\, r_t\, \mathrm{d}\tau + \int_{-\psi}^{\psi} \tilde{Q}_\tau \tilde{H}_{\theta\tau}^{TT}\, r_t\, \mathrm{d}\tau\right), \tag{33}$$

where $\tilde{H}_{\theta\tau}^{NN}$, $\tilde{H}_{\theta\tau}^{NT}$, $\tilde{H}_{\theta\tau}^{TN}$, $\tilde{H}_{\theta\tau}^{TT}$ are the FRFs of the PiP model and express the displacement at angle θ for a unit load applied at angle τ. The left superscript determines the direction, where the load at angle θ is applied. N is normal to the tunnel wall and T is tangential. The right superscript determines the direction of the calculated displacement at angle τ.

The integrations in the previous equations can be performed numerically. The trapezium rule [20] is used, where the collocation points are evenly distributed along the integration path. Eqs. (27)–(29) can be written as

$$\tilde{y}_3 = \tilde{H}_v\left(\tilde{G}_{r1} + \tilde{G}_{r2} - \sum_{j=1}^{M} c_j \tilde{P}_j \cos\theta_j\, r_t \Delta\theta - \sum_{j=1}^{M} c_j \tilde{Q}_j \sin\theta_j\, r_t \Delta\theta\right), \tag{34}$$

$$\tilde{y}_4 = \tilde{H}_h\left(\sum_{j=1}^{M} c_j \tilde{P}_j \sin\theta_j\, r_t \Delta\theta - \sum_{j=1}^{M} c_j \tilde{Q}_j \cos\theta_j\, r_t \Delta\theta\right) \tag{35}$$

and

$$\tilde{y}_5 = \tilde{H}_\gamma \left\{ [\tilde{G}_{r1} - \tilde{G}_{r2}] a_t - \sum_{j=1}^{M} c_j \tilde{P}_j (r_t - b_b) \sin\,\theta_j \, r_t \Delta\theta - \sum_{j=1}^{M} c_j \tilde{Q}_j [r_t - (r_t - b_b)\cos\,\theta_j] r_t \Delta\theta \right\}, \tag{36}$$

where M is the number of collocation points, $c_j = 0.5$ for $j = 1$, M and $c_j = 1$ for all other j, $\Delta\theta = 2\psi/(M-1)$ and $\theta_j = -\psi + (j-1)\Delta\theta$.

Using the same collocation points as in Eqs. (34)–(36), Eqs. (32) and (33) can be written as

$$\tilde{y}_{iN} = \left(\sum_{j=1}^{M} c_j \tilde{P}_j \tilde{H}_{ij}^{NN} \, r_t \Delta\theta + \sum_{j=1}^{M} c_j \tilde{Q}_j \tilde{H}_{ij}^{NT} \, r_t \Delta\theta \right) \tag{37}$$

and

$$\tilde{y}_{iT} = \left(\sum_{j=1}^{M} c_j \tilde{P}_j \tilde{H}_{ij}^{TN} \, r_t \Delta\theta + \sum_{j=1}^{M} c_j \tilde{Q}_j \tilde{H}_{ij}^{TT} \, r_t \Delta\theta \right). \tag{38}$$

Note that $\Delta\tau$ is replaced by $\Delta\theta$ in the previous equations as the same collocation points are used for all numerical integrations, i.e. $\Delta\tau = \Delta\theta$.

To calculate the displacements of the track and the PiP model, equations of equilibrium are written in matrix form as done in the previous two sections. Eqs. (16)–(20) can be written again here to calculate the model displacements. Some notation of these equations is different and is defined as

$$\tilde{\mathbf{P}} = [\tilde{P}_1, \tilde{P}_2, \ldots, \tilde{P}_M, \tilde{Q}_1, \tilde{Q}_2, \ldots, \tilde{Q}_M]^{\mathrm{T}},$$

$\tilde{\mathbf{H}}_{21}$ is $3 \times 2M$ matrix and can be written as

$$\tilde{\mathbf{H}}_{21} = \left[\tilde{\mathbf{H}}_{21}^{11}, \tilde{\mathbf{H}}_{21}^{12} \right],$$

where

$$\tilde{\mathbf{H}}_{21}^{11} = r_t \Delta\theta \begin{bmatrix} -c_1 H_v \cos\,\theta_1 & -c_2 H_v \cos\,\theta_2 & \ldots & -c_M H_v \cos\,\theta_M \\ c_1 H_h \sin\,\theta_1 & c_2 H_h \sin\,\theta_2 & \ldots & c_M H_h \sin\,\theta_M \\ -c_1 \tilde{H}_\gamma (r_t - b_b) \sin\,\theta_1 & -c_2 \tilde{H}_\gamma (r_t - b_b) \sin\,\theta_2 & \ldots & -c_M \tilde{H}_\gamma (r_t - b_b) \sin\,\theta_M \end{bmatrix},$$

$$\tilde{\mathbf{H}}_{21}^{12} = r_t \Delta\theta \begin{bmatrix} -c_1 H_v \sin\,\theta_1 & -c_2 H_v \sin\,\theta_2 & \ldots & -c_M H_v \sin\,\theta_M \\ -c_1 H_h \cos\,\theta_1 & -c_2 H_h \cos\,\theta_2 & \ldots & -c_M H_h \cos\,\theta_M \\ -c_1 \tilde{H}_\gamma [r_t - (r_t - b_b)\cos\,\theta_1] & -c_2 \tilde{H}_\gamma [r_t - (r_t - b_b)\cos\,\theta_2] & \ldots & -c_M \tilde{H}_\gamma [r_t - (r_t - b_b)\cos\,\theta_M] \end{bmatrix}.$$

$\tilde{\mathbf{H}}_{41}$ is $2M \times 3$ matrix and can be written as

$$\tilde{\mathbf{H}}_{41} = \begin{bmatrix} \tilde{\mathbf{H}}_{41}^{11} \\ \tilde{\mathbf{H}}_{41}^{21} \end{bmatrix},$$

where

$$\tilde{\mathbf{H}}_{41}^{11} = k_n \begin{bmatrix} \cos\,\theta_1 & -\sin\,\theta_1 & (r_t - b_b)\sin\,\theta_1 \\ \cos\,\theta_2 & -\sin\,\theta_2 & (r_t - b_b)\sin\,\theta_2 \\ \vdots & \vdots & \vdots \\ \cos\,\theta_M & -\sin\,\theta_M & (r_t - b_b)\sin\,\theta_M \end{bmatrix},$$

$$\tilde{\mathbf{H}}_{41}^{21} = k_s \begin{bmatrix} \sin\theta_1 & \cos\theta_1 & r_t - (r_t - b_b)\cos\theta_1 \\ \sin\theta_2 & \cos\theta_2 & r_t - (r_t - b_b)\cos\theta_2 \\ \vdots & \vdots & \vdots \\ \sin\theta_M & \cos\theta_M & r_t - (r_t - b_b)\cos\theta_M \end{bmatrix},$$

$\tilde{\mathbf{H}}_{42}$ is $2M \times 2M$ matrix and can be written as

$$\tilde{\mathbf{H}}_{42} = \begin{bmatrix} \tilde{\mathbf{H}}_{42}^{11} & \tilde{\mathbf{H}}_{42}^{12} \\ \tilde{\mathbf{H}}_{42}^{21} & \tilde{\mathbf{H}}_{42}^{22} \end{bmatrix},$$

where $\tilde{\mathbf{H}}_{42}^{11} = -k_n \mathbf{I}_{2M}$, $\tilde{\mathbf{H}}_{42}^{12} = \mathbf{Z}(M, M)$, $\tilde{\mathbf{H}}_{42}^{21} = \mathbf{Z}(M, M)$ and $\tilde{\mathbf{H}}_{42}^{22} = -k_s I_{2M}$. $\mathbf{Z}(M,M)$ is $M \times M$ matrix with zero elements.

$\tilde{\mathbf{H}}_{51}$ is $2M \times 2M$ matrix and can be written as

$$\tilde{\mathbf{H}}_{51} = \begin{bmatrix} \tilde{\mathbf{H}}_{51}^{11} & \tilde{\mathbf{H}}_{51}^{12} \\ \tilde{\mathbf{H}}_{51}^{21} & \tilde{\mathbf{H}}_{51}^{22} \end{bmatrix},$$

where

$$\tilde{\mathbf{H}}_{51}^{11} = r_t \Delta\theta \begin{bmatrix} c_1 H_{11}^{NN} & c_2 H_{12}^{NN} & \dots & c_M H_{1M}^{NN} \\ c_1 H_{21}^{NN} & c_2 H_{22}^{NN} & \dots & c_M H_{2M}^{NN} \\ \vdots & \vdots & \vdots & \vdots \\ c_1 H_{M1}^{NN} & c_2 H_{M2}^{NN} & \dots & c_{MM} H_{MM}^{NN} \end{bmatrix},$$

$$\tilde{\mathbf{H}}_{51}^{12} = r_t \Delta\theta \begin{bmatrix} c_1 H_{11}^{NT} & c_2 H_{12}^{NT} & \dots & c_M H_{1M}^{NT} \\ c_1 H_{21}^{NT} & c_2 H_{22}^{NT} & \dots & c_M H_{2M}^{NT} \\ \vdots & \vdots & \vdots & \vdots \\ c_1 H_{M1}^{NT} & c_2 H_{M2}^{NT} & \dots & c_{MM} H_{MM}^{NT} \end{bmatrix},$$

$$\tilde{\mathbf{H}}_{51}^{21} = r_t \Delta\theta \begin{bmatrix} c_1 H_{11}^{TN} & c_2 H_{12}^{TN} & \dots & c_M H_{1M}^{TN} \\ c_1 H_{21}^{TN} & c_2 H_{22}^{TN} & \dots & c_M H_{2M}^{TN} \\ \vdots & \vdots & \vdots & \vdots \\ c_1 H_{M1}^{TN} & c_2 H_{M2}^{TN} & \dots & c_{MM} H_{MM}^{TN} \end{bmatrix},$$

$$\tilde{\mathbf{H}}_{51}^{22} = r_t \Delta\theta \begin{bmatrix} c_1 H_{11}^{TT} & c_2 H_{12}^{TT} & \dots & c_M H_{1M}^{TT} \\ c_1 H_{21}^{TT} & c_2 H_{22}^{TT} & \dots & c_M H_{2M}^{TT} \\ \vdots & \vdots & \vdots & \vdots \\ c_1 H_{M1}^{TT} & c_2 H_{M2}^{TT} & \dots & c_{MM} H_{MM}^{TT} \end{bmatrix}.$$

The model displacements can now be calculated from the following equations, compare with Eqs. (24)–(26):

$$\tilde{\mathbf{y}}_{\mathbf{s}} = [\mathbf{I}_3 - \tilde{\mathbf{H}}_{22}(\mathbf{I}_2 - \tilde{\mathbf{H}}_{31}\tilde{\mathbf{H}}_{11})^{-1}\tilde{\mathbf{H}}_{32} - \tilde{\mathbf{H}}_{21}(\mathbf{I}_{2M} - \tilde{\mathbf{H}}_{42}\tilde{\mathbf{H}}_{51})^{-1}\tilde{\mathbf{H}}_{41}]^{-1}\tilde{\mathbf{H}}_{22}(\mathbf{I}_2 - \tilde{\mathbf{H}}_{31}\tilde{\mathbf{H}}_{11})^{-1}\tilde{\mathbf{H}}_{31}\tilde{\mathbf{H}}_{12}\tilde{\mathbf{F}}_{\mathbf{R}}, \quad (39)$$

$$\tilde{\mathbf{P}} = (\mathbf{I}_{2M} - \tilde{\mathbf{H}}_{42}\tilde{\mathbf{H}}_{51})^{-1}\tilde{\mathbf{H}}_{41}\tilde{\mathbf{y}}_{\mathbf{s}} \quad (40)$$

and

$$\tilde{\mathbf{y}}_{\mathbf{T}} = \tilde{\mathbf{H}}_{51}\tilde{\mathbf{P}}. \tag{41}$$

3. Evaluation of FRFs

To calculate the displacements at a given wavenumber and angular frequency (ξ,ω) for any of the models described in the previous sections, values of FRFs are to be calculated firstly at the same wavenumber and angular frequency. FRF of the rails is calculated in bending only while FRFs of the slab are calculated in both bending and torsion. FRFs of the coupled tunnel and the surrounding soil are calculated using the PiP model.

3.1. FRFs of the rails and slab in bending

The rails and the slab are modelled as Euler–Bernoulli beams in bending. The governing differential equation for an infinite Euler–Bernoulli beam subjected to external force $F(x,t)$ is given by

$$EI\frac{\partial^4 y}{\partial x^4} + m\frac{\partial^2 y}{\partial t^2} = F(x,t), \tag{42}$$

where EI is the bending stiffness of the beam and m is the mass of beam per unit length. Transforming this equation to the wavenumber–frequency domain results in

$$EI\xi^4\tilde{y} - m\omega^2\tilde{y} = \tilde{F}. \tag{43}$$

The FRF for the beam bending is defined as the beam displacement due to a unit force in the wavenumber–frequency domain. Applying this definition results in

$$\tilde{H}_y = \frac{\tilde{y}}{\tilde{F}} = \frac{1}{EI\xi^4 - m\omega^2}. \tag{44}$$

3.2. FRFs of the slab in torsion

The classical theory of torsion is applied using St. Venant hypothesis. This assumes warping free cross-sections. The governing differential equation for an infinite beam subjected to external torque $T(x,t)$ is given by

$$J\frac{\partial^2 \gamma}{\partial t^2} - GK\frac{\partial^2 \gamma}{\partial x^2} = T(x,t), \tag{45}$$

where GK is the torsional rigidity of the beam (G is the shear modulus, K the torsion constant of the beam section), and J the polar moment of inertia. Transforming this equation to the wavenumber–frequency domain results in

$$-J\omega^2\tilde{\gamma} + GK\xi^2\tilde{\gamma} = \tilde{T}. \tag{46}$$

The FRF for the beam torsion is defined as the beam rotation for a unit torque in the wavenumber–frequency domain. Applying this definition results in

$$\tilde{H}_\gamma = \frac{\tilde{\gamma}}{\tilde{T}} = \frac{1}{GK\xi^2 - J\omega^2}. \tag{47}$$

3.3. FRFs of the PiP model

Unlike FRFs of beams, calculating FRFs of the PiP model are not straightforward. This is because another coordinate is involved in the calculations. This coordinate is θ and it describes the variation around the tunnel. There are two types of FRFs according to the input load. In the first type, the input load is applied radially to the tunnel wall, for instance to calculate $\tilde{H}_{6-6}$, $\tilde{H}_{7-6}$, $\tilde{H}_{8-6}$ and $\tilde{H}_{9-6}$ in Section 2.1 (see Fig. 2d). In the

second type, the input load is applied tangentially to the tunnel wall, for instance to calculate $\tilde{H}_{6-8}$, $\tilde{H}_{7-8}$, $\tilde{H}_{8-8}$ and $\tilde{H}_{9-8}$ in Section 2.1 (see Fig. 2d). The difference between the two types is that the load and displacements in the first type decompose into symmetrical-sinusoidal Fourier-series components, while the second results in anti-symmetrical–sinusoidal Fourier-series components about the axis-of-symmetry of the PiP model at the load position. To explain this point, consider calculations of $\tilde{H}_{7-8}$. This FRF can be evaluated by the following:

- apply a unit force in the position and the direction of y_8 (see Fig. 2d) in the form $F(x,t) = 1e^{(i\bar{\xi}x+\omega t)}$;
- calculate the displacement in the position and the direction of y_7 (see Fig. 2d). The displacement takes the form $y_7(x,t) = \tilde{H}_{7-8}e^{(i\bar{\xi}x+\omega t)}$.

As discussed in Ref. [19], a unit load in the wavenumber–frequency domain at $[\xi = \bar{\xi}$ and $\omega = \bar{\omega}]$ corresponds to a load with space and time variation $e^{(i\bar{\xi}x+\bar{\omega}t)}$ in the space–time domain. Transforming the quantity $[1\delta(\xi-\bar{\xi})\delta(\omega-\bar{\omega})]$ to the space–time domain confirms this result.

To include the variation around the tunnel wall, the load $F(x,t) = 1e^{(i\bar{\xi}x+\omega t)}$ can be written in a vector form to express the longitudinal, the tangential and the radial load distribution in terms of θ as

$$\mathbf{F}(x,\theta,t) = \begin{bmatrix} 0 \\ \delta(\theta)/r_t \\ 0 \end{bmatrix} e^{(i\bar{\xi}x+\omega t)}, \tag{48}$$

where θ is measured in a clockwise direction and is equal to zero at the position of the applied load. The distribution with respect to θ can be written as a summation of Fourier series, see Ref. [20] for example, with periodicity 2π. This is because the load does not change by moving from θ to $\theta+2\pi$ around the tunnel. Therefore, Eq. (48) can be written as

$$\mathbf{F}(x,\theta,t) = \sum_{n=0}^{\infty} \begin{bmatrix} c_{xn}\sin n\theta \\ c_{\theta n}\cos n\theta \\ c_{rn}\sin n\theta \end{bmatrix} e^{i(\xi x+\omega t)}, \tag{49}$$

where $c_{\theta 0} = 1/2\pi r_t$ and $c_{\theta n} = 1/\pi r_t$ for $n = 1,2,\ldots,\infty$, $c_{xn} = 0$ and $c_{rn} = 0$ for all n.

It should be noted that the load components in Eq. (49) for a given cross-sectional wavenumber n, is anti-symmetrical about $\theta = 0$ and is identified in this context as the second loading combination. The first loading combination, i.e. a symmetrical input load, is calculated by replacing any $\cos n\theta$ in Eq. (49) by $\sin n\theta$ and vice versa. For general anti-symmetrical stresses applied on the PiP model in the form:

$$\mathbf{q}(x,\theta,t) = \begin{bmatrix} q_x \\ q_\theta \\ q_r \end{bmatrix} = \begin{bmatrix} \tilde{q}_x\sin n\theta \\ \tilde{q}_\theta\cos n\theta \\ \tilde{q}_r\sin n\theta \end{bmatrix} e^{i(\xi x+\omega t)}. \tag{50}$$

The displacement of the PiP model at the inner surface of the tunnel wall can be written in the form:

$$\mathbf{u}(x,\theta,t) = \begin{bmatrix} u_x \\ u_\theta \\ u_r \end{bmatrix} = \begin{bmatrix} \tilde{u}_x\sin n\theta \\ \tilde{u}_\theta\cos n\theta \\ \tilde{u}_r\sin n\theta \end{bmatrix} e^{i(\xi x+\omega t)}. \tag{51}$$

Fig. 5 shows the sign convention for the stresses and displacements in Eqs. (50) and (51). It also shows the composition of a tangential load applied at the tunnel invert into its Fourier components. The PiP model displacements due to the load in Eq. (49) can be calculated using Eqs. (50) and (51) for each n, in which $\tilde{u}_x$, $\tilde{u}_\theta$ and $\tilde{u}_z$ are significant. The total displacement is calculated by summing the displacements for all values of n.

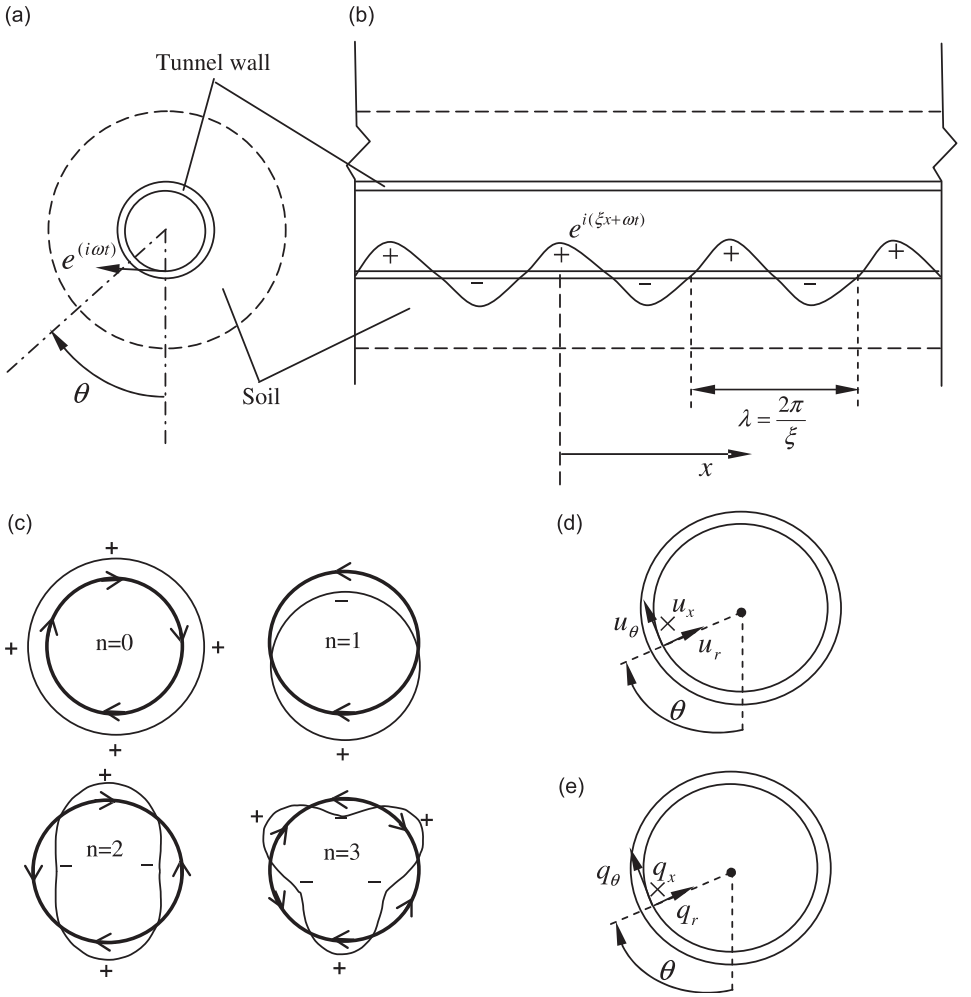

Fig. 5. Schematic showing the decomposition of a load $e^{i(\omega t+\xi x)}$ applied tangentially at the tunnel invert: (a, b) show the spatial distribution of the load, (c) shows the steady state and the first three Fourier components of the load. (d, e) Show the sign convention of the displacements and stresses respectively. The cross sign means perpendicular to the page, into it.

The PiP model displacement given by Eq. (51) decreases by increasing the value of n and hence a limited number of n should be included in the calculations to get a converged solution. More details about the PiP model and the FRF for symmetrical and anti-symmetrical inputs are given in Section 5.

4. Stiffness of slab bearings

The stiffness of slab bearings is expressed in terms of the vertical natural frequency of the slab modelled as a beam on Winkler foundation, where the foundation stiffness is equal to the stiffness of the slab bearings. This is a widely accepted way in the industry to describe floating-slab tracks. A f_n Hz floating slab is a slab that has a cut-on frequency at f_n Hz for a rigid tunnel wall. It should be noted that in reality the vertical cut-on frequency of the slab is shifted due to the influence of the rails, tunnel and ground, which are not considered when calculating the cut-on frequency. However, this shift is typically small for soft slab bearings and much lighter rails compared with the slab. For a floating slab with a mass m_s and vertical stiffness of slab bearings k_v, the cut-on frequency is calculated from the following

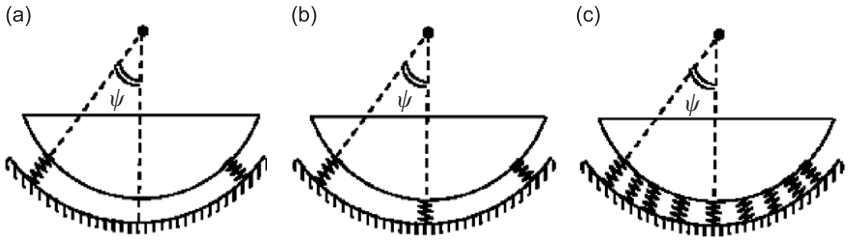

Fig. 6. 2D models of floating slabs connected to the tunnel wall via: (a) two lines of support, (b) three lines of support and (c) uniform support.

relationship:

$$f_n = \frac{1}{2\pi}\sqrt{\frac{k_v}{m_s}}. \tag{52a}$$

Using Eq. (52a) for the models shown in Fig. 6, the calculated natural frequency of the floating slabs are: for two lines of support:

$$f_n = \frac{1}{2\pi}\sqrt{\frac{k_n(2\cos^2\psi + 2\Re\sin^2\psi)}{m_s}}, \tag{52b}$$

for three lines of support:

$$f_n = \frac{1}{2\pi}\sqrt{\frac{k_n(2\cos^2\psi + 1 + 2\Re\sin^2\psi)}{m_s}}, \tag{52c}$$

for uniform support:

$$f_n = \frac{1}{2\pi}\sqrt{\frac{r_t k_n[\psi(1+\Re) + 0.5(1-\Re)\sin 2\psi]}{m_s}}, \tag{52d}$$

where $\Re$ is the ratio of the shear stiffness to the normal stiffness of the slab bearings, i.e. $\Re = k_s/k_n$.

A directly-fixed slab can be modelled by using the uniform support and setting the natural frequency to a number much greater than the highest frequency of interest in the analysis.

5. Dispersion characteristics of the model

In this section, FRFs of the model are investigated by studying the dispersion characteristics of the PiP model and the track on rigid foundation model. It is useful before that to study the dispersion behaviour of the separate components of the PiP model, i.e. the free tunnel modelled as a thin shell and the free soil modelled as a full-space with a cylindrical cavity. The reader is referred to Refs. [19,21,22] which provide a good introduction about wave propagation and dispersion equations.

As will be seen in this section, damping is set to zero when studying the dispersion characteristic of models. This is done when solving the dispersion equation and also when plotting FRFs in the wavenumber–frequency domain. Introducing damping attenuates the peaks at the dispersion curves (as propagating waves gain an attenuation factor) and makes propagating solutions less easy to identify in FRF plots. Note that damping should be introduced when transforming results to the space domain to transform infinite peaks at dispersion curves to finite ones.

Table 1 shows the parameters of the tunnel, soil and track, which are used for the analysis in the following sections. The parameters used in the table are defined as follows: E is the elastic modulus; v the Poisson's ratio; ρ is the density; r_c is the cavity radius; λ and μ are Lame's constants; c_p and c_s are the compression and shear wave velocities; a is the tunnel mean radius and h is the tunnel thickness. The track parameters are defined in Section 2.

Table 1
Parameter values used to model a railway track in a tunnel

Soil	Tunnel	Track
$E = 550 \times 10^6$ Pa	$E = 50 \times 10^9$ Pa	$EI_r = 5 \times 10^6$ Pa m^4
$\nu = 0.44$	$\nu = 0.3$	$m_r = 50$ kg/m
$\rho = 2000$ kg/m^3	$\rho = 2500$ kg/m^3	$k_r = 20 \times 10^6$ N/m/m
$r_c = 3.00$ m	$r_t = 2.75$ m	$EI_v = 1430 \times 10^6$ Pa m^4
$\lambda = 1.4 \times 10^9$ Pa	$h = 0.25$ m	$EI_h = 41699 \times 10^6$ Pa m^4
$\mu = 191 \times 10^6$ Pa	$\lambda = 28.8 \times 10^9$ Pa	$m_s = 3500$ kg/m
$c_p = 944$ m/s	$\mu = 19.2 \times 10^9$ Pa	$GK = 1.875 \times 10^9$ Pa m^4
$c_s = 309$ m/s	$c_p = 5189$ m/s	$J = 1310$ kg m^2/m
	$c_s = 2774$ m/s	$a_t = 0.75$ m
		$b_t = 0.2$ m
		$b_b = 0.3$ m
		$\Re = 1.0$ for $f_n \to \infty$ and $\Re = 0.5$ otherwise

5.1. Dispersion characteristics of the PiP model

This section is divided into three parts discussing the solution of the dispersion equations for: the tunnel wall modelled as a thin shell, the surrounding soil modelled using the elastic continuum theory and the coupled tunnel wall and soil.

6. The tunnel wall modelled as a thin shell

The equilibrium equation of a thin cylindrical shell in the wavenumber–frequency domain is given by

$$[\mathbf{A}]\begin{bmatrix}\tilde{u}_{xn}\\ \tilde{u}_{\theta n}\\ \tilde{u}_{rn}\end{bmatrix} = \frac{-a(1-\nu^2)}{Eh}\begin{bmatrix}\tilde{q}_{xn}\\ \tilde{q}_{\theta n}\\ \tilde{q}_{rn}\end{bmatrix}, \tag{53}$$

where $\mathbf{A} = \mathbf{A}_1$ for the first loading combination, i.e. symmetrical input (see Eq. (6) of Ref. [9]) and $\mathbf{A} = \mathbf{A}_2$ for the second loading combination, i.e. anti-symmetrical input. The elements of $\mathbf{A}_2$ are calculated by the authors as shown in Appendix A, while the elements of $\mathbf{A}_1$ are calculated by Forrest and Hunt [9] and can be written in terms of $\mathbf{A}_2$ elements as follows:

$$\mathbf{A}_1 = \begin{bmatrix}1 & -1 & 1\\ -1 & 1 & -1\\ 1 & -1 & 1\end{bmatrix} * \mathbf{A}_2, \tag{54}$$

where $(*)$ means an element to element multiplication. The unforced vibration (free vibration) solution of Eq. (53) is calculated by setting the stress vector to zero, this results in two possible solutions:

$$\begin{aligned}&\text{a trivial solution, i.e. } \tilde{u}_{xn} = 0,\ \tilde{u}_{\theta n} = 0,\ \tilde{u}_{rn} = 0,\\ &\text{a non-trivial solution, i.e. } D(\xi,\omega) = |\mathbf{A}| = 0.\end{aligned} \tag{55}$$

It can be shown that the determinants of $\mathbf{A}_1$ and $\mathbf{A}_2$ are identical by calculating the determinants of both the matrices. It can be alternatively shown by using the following determinants property. For two square matrices $\mathbf{B}$ and $\mathbf{G}$ of the same size, if $\mathbf{B}$ results from multiplying one of $\mathbf{G}$'s rows or columns by a constant c, then the relationship between the determinants of the two matrices is, see Ref. [23], for example

$$|\mathbf{B}| = c|\mathbf{G}|. \tag{56}$$

Note that $\mathbf{A}_1$ is calculated by multiplying the second row and then the second column of $\mathbf{A}_2$ by -1 and hence the two matrices have the same determinant. Eq. (55) is known as the dispersion equation. This equation can

be written as a polynomial of the eighth degree as

$$D(\xi,\omega) = a_1\xi^8 + a_2\xi^6 + a_3\xi^4 + a_4\xi^2 + a_5, \tag{57}$$

where a_1, a_2, a_3, a_4 and a_5 are real quantities (for no damping) and are functions of the angular frequency ω, the cross-sectional wavenumber n and the shell parameters.

For given n and ω, there are eight roots for Eq. (57). If ξ is a root, $-\xi$ is also a root due to absence of odd powers in Eq. (57). Also ξ^* is another root because the coefficients $a_1, a_2, \ldots, a_5$ are real quantities. This means for each root ξ, there are three other roots $[-\xi, \xi^*, -\xi^*]$. Note that for real values of ω, if the value of ξ is real then it is represents a propagating wave due to the factor $e^{i(\omega t+\xi x)}$. An imaginary and a complex value of ξ represent an evanescent wave and a leaky wave, respectively, see Appendix A of Ref. [19] for example.

Fig. 7 shows the solutions of the dispersion equation calculated by Matlab [24] built-in function ''roots'' for the tunnel parameters given in Table 1. For $n = 0$, there are no evanescent waves at the frequency range of interest. Two non-dispersive waves can propagate freely at all frequencies: the compression wave and the shear wave (torsional wave). The compression wave propagates with phase velocity equal to $\sqrt{E/\rho} = 4472\,\text{m/s}$ and this is equal to the pressure wave velocity of cylinders [25] and is slower than the velocity of compression wave in a full-space (5189 m/s) with the same material properties as the shell (see Table 1). This is because Poisson's effect is restraint in a full-space while it is not in the shell case. Unlike the compression wave, the torsional wave propagates with velocity equal to the shear wave velocity in a full-space, which is equal to 2774 m/s.

For $n = 1$, there are propagating waves at all frequencies while evanescent waves exist below 153.5 Hz with wavenumbers smaller than 0.16 rad/m. Leaky waves exist at all frequencies. The real parts of wavenumbers associated with the leaky waves are greater than the wavenumbers of the propagating waves and hence leaky waves have smaller wavelengths compared with the propagating waves. The imaginary parts of wavenumbers associated with the leaky waves are greater than wavenumbers for evanescent waves and hence they are much attenuated. At 153.6 Hz, there is a cut-on frequency, above which two waves with different wavelengths propagate. The case for $n = 2$ is important, because it is the minimum cross-sectional wavenumber in which waves do not propagate below a certain frequency (17.5 Hz in this case).

Fig. 8a shows the dispersion curves for all values of n. For values of n greater than 5, waves cannot propagate freely within the frequency range of interest. The curves in Fig. 8a are assembled using the real solutions for the range $n = 0$–5. Dispersion curves are of particular interest, as FRFs in the wavenumber–frequency domain exhibit peaks (or infinite response in absence of damping) at wavenumbers and angular frequencies along these curves. Also the velocity lines can be constructed to identify the peaks in the space–time domain [19].

The cut-on frequencies of the thin shell are associated with zero wavenumbers, i.e. a plane-strain problem. Hence, the shell behaves as a 2D ring and cut-on frequencies can be calculated from the corresponding natural frequencies of a ring as verified by Forrest and Hunt [9].

Fig. 8b shows the dispersion curves of the tunnel modelled as a thick cylindrical shell using the elastic continuum theory. The work of Gazis [26–28] is employed to calculate these results. Gazis uses the elastic continuum theory to calculate dispersion curves for cylindrical shells. The formulation is the same as presented by Forrest and Hunt [9]. However, Gazis uses both the Bessel and the modified Bessel functions to solve the differential equations and this leads to dispersion equation with pure-real values but Forrest and Hunt use only the modified Bessel functions to solve differential equations of the shell and this leads to dispersion equation with complex values at some wavenumbers and angular frequencies. Both formulations are used in this work; Gazis' formulation and Forrest and Hunt's formulation. Identical results are obtained (see Fig. 8b). For Forrest and Hunt's formulation, the dispersion equation is calculated by solving the following equation (see Eq. (31) in Ref. [9]):

$$\begin{vmatrix} [\mathbf{T}_r]_{r=a-h/2} \\ [\mathbf{T}_r]_{r=a+h/2} \end{vmatrix} = 0. \tag{58}$$

It can be proven, in the same way as done for Eq. (55), that Eq. (58) results in the same expression whether the first or the second loading combination is used. The dispersion equation is solved by using Newton–Raphson method. Details of this method are found in the next section. By comparing Fig. 8a and

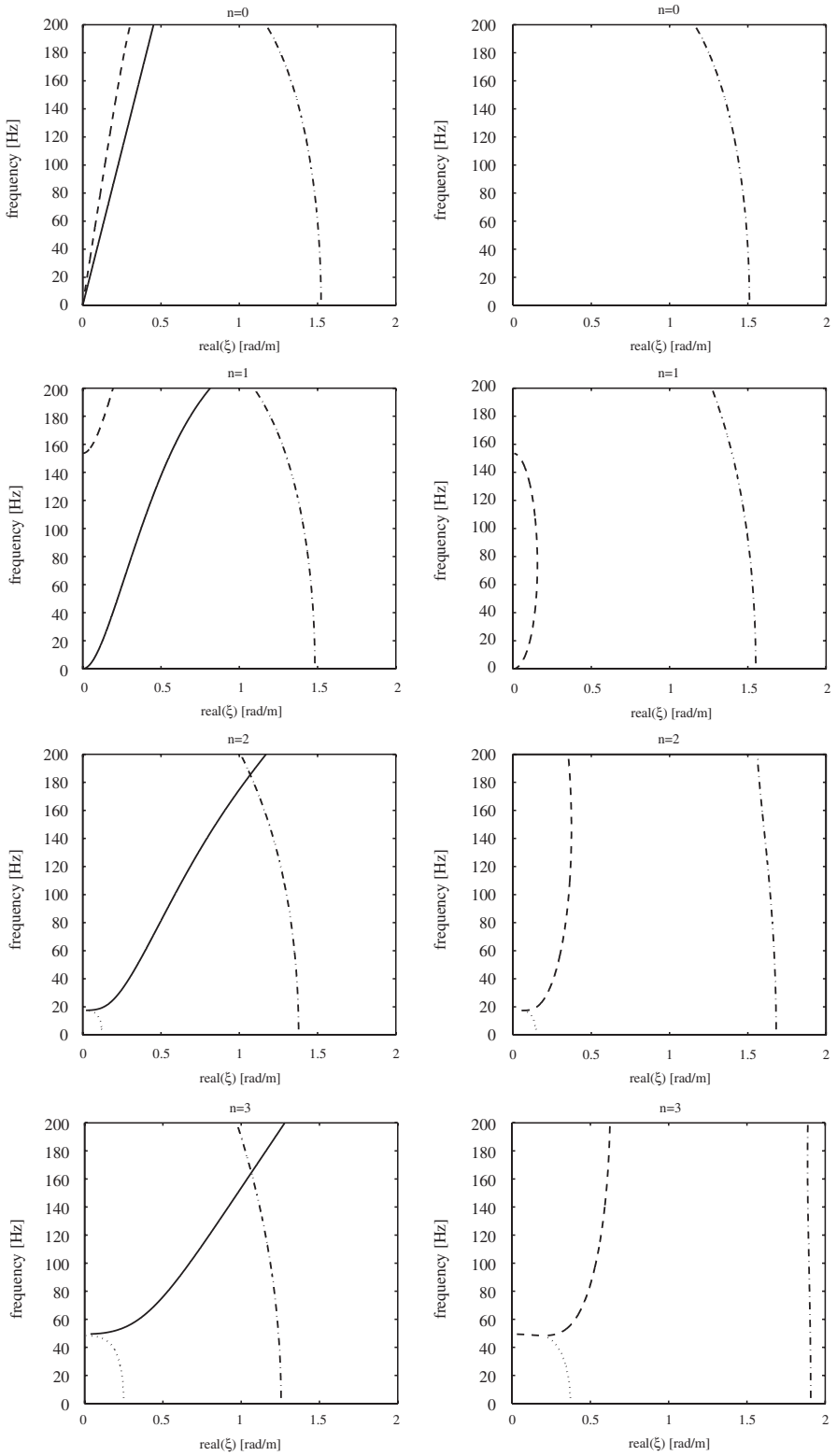

Fig. 7. Solutions of the dispersion equation of a thin shell, where only roots in the first quarter of the complex wavenumbers for $n = [0,1,2,3]$ are plotted. The left column of subfigures shows the real part of the roots, where the right column shows the imaginary part of the roots. Each root is plotted with different line style, i.e. (-), (--), (-.) and (..).

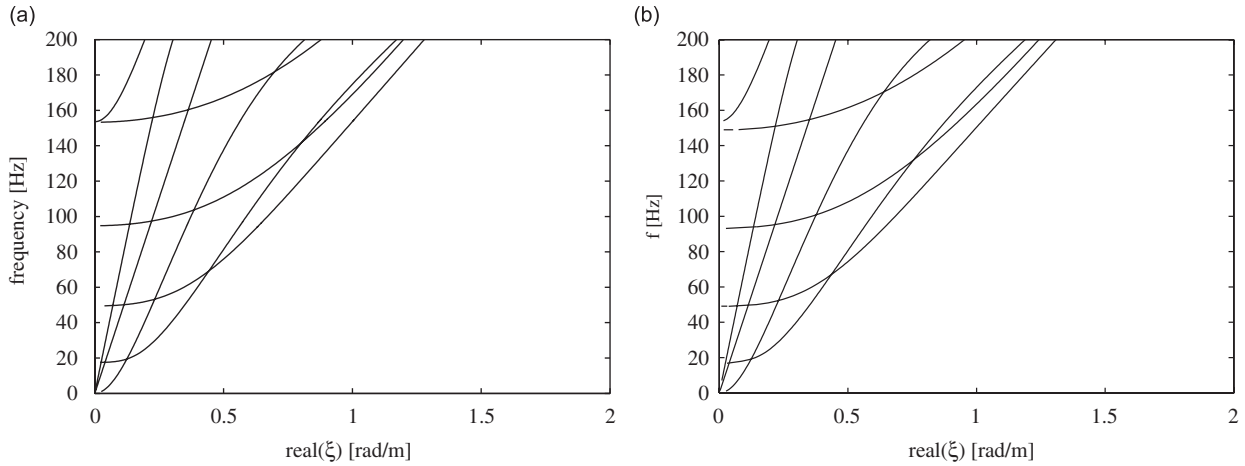

Fig. 8. Dispersion curves of a free tunnel wall modelled as (a) thin shell and (b) thick shell using the elastic continuum theory.

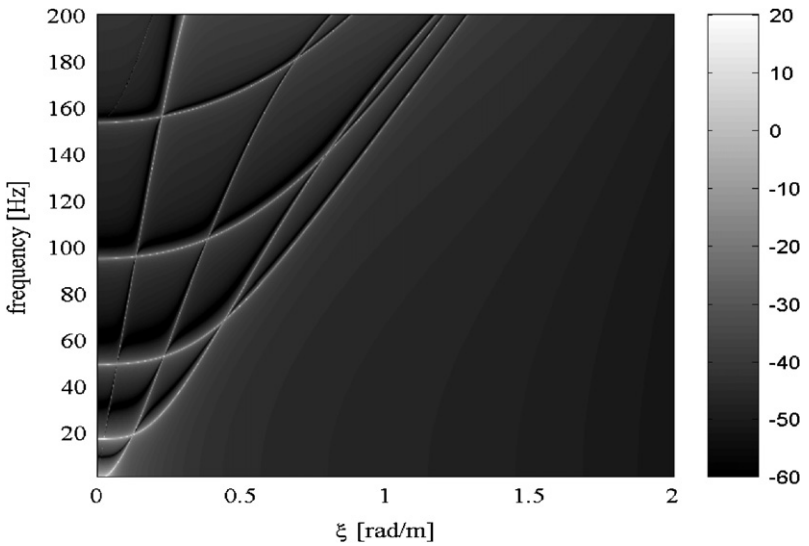

Fig. 9. Radial displacement FRF of the free tunnel wall at $\theta = 0$ under a radial load.

b, it can be seen that the dispersion curves are calculated with good accuracy using the thin shell formulation in the range of frequency of interest.

Fig. 9 shows the radial FRF of a thin shell calculated for a radial load $e^{i(\omega t+\xi x)}$ applied at $\theta = 0$, where the response is calculated at the excitation line. It can be seen that peaks occur at the dispersion curves as shown in Fig. 8a with no torsional waves propagating for $n = 0$ as shown in Fig. 8a. This is because torsional waves are not excited by radial loads.

Fig. 10a shows the displacement at $x = 0$, $\theta = 0$, for a radial harmonic load applied at $x = 0$ with circumferential distribution $\cos(2\theta)$. Damping is introduced to the shell by using a complex modulus of elasticity. This is done by replacing E by E_2 in Eq. (53), where $E_2 = E(1 + i\eta_E)$, η_E is the hysteretic loss factor and is taken equal to 5%. The discrete Fourier transform DFT [29] is used to transform results from the wavenumber domain to the space domain with spatial interval $dx = 0.25$ m and number of points $N = 2^{14}$. A peak occurs at 17.5 Hz corresponding to the cut-on frequency for $n = 2$ in Fig. 7.

To examine the existence of propagating waves, the response is calculated away from the excitation point with a distance sufficient to allow decaying of evanescent and leaky waves. In Fig. 11a, the displacement is

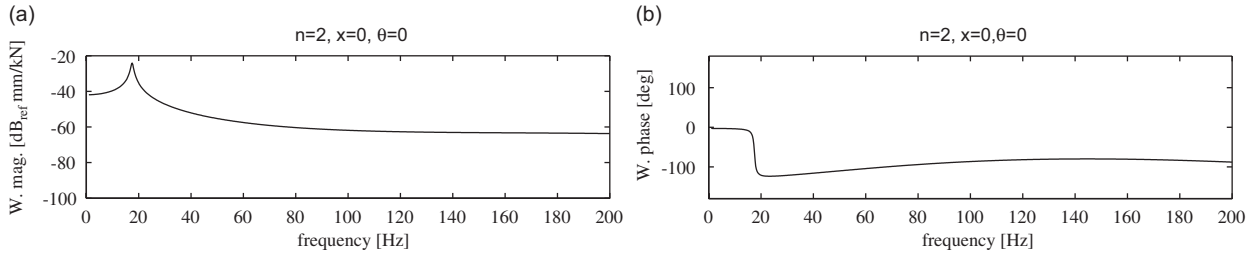

Fig. 10. The response at the excitation point of a free tunnel wall modelled as a thin shell for radial input at $x = 0$ with $n = 2$; (a) displacement and (b) phase.

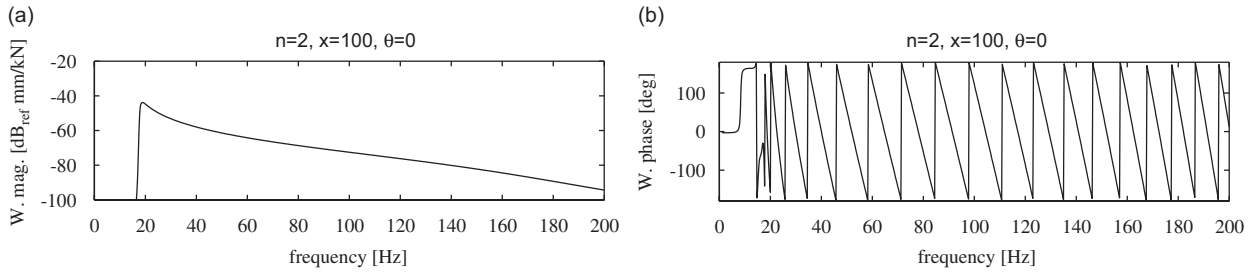

Fig. 11. The response at 100 m away from the excitation point of an isolated tunnel wall modelled as a thin shell for radial input with $n = 2$; (a) displacement and (b) phase.

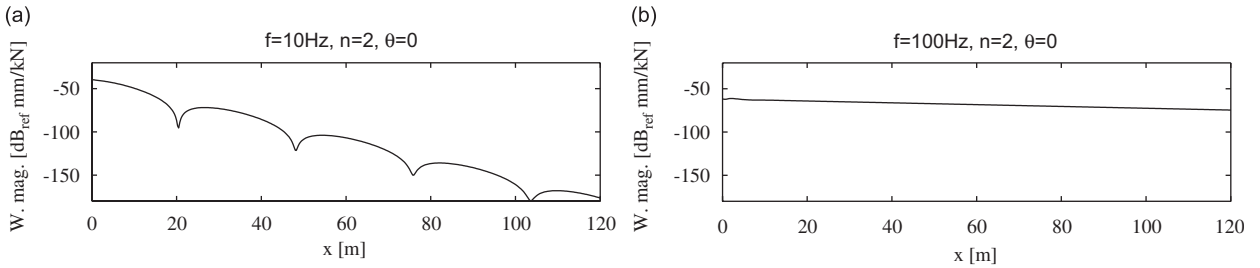

Fig. 12. The isolated thin shell response along the shell with $\theta = 0$ for a radial harmonic load applied at $x = 0$ with $n = 2$ and excitation frequency: (a) 10 Hz and (b) 100 Hz.

calculated at 100 m away from the excitation point. It is clear that the response is small below the cut-on frequency. Fig. 11b shows the phase calculated at this point. The phase fluctuates around the zero value and less fluctuation is expected for results calculated at further distance from the excitation point. This can be explained by calculating the rate of change of phase with respect to frequency, which can be expressed as

$$\frac{\mathrm{d}\varphi}{\mathrm{d}f} = -\frac{\mathrm{d}(2\pi L/\lambda)}{\mathrm{d}f} = \frac{-2\pi L}{c_g}, \tag{59}$$

where φ is the phase of the measuring point, c_g is the group velocity, λ is the wavenumber and L is the distance between the excitation point and the measuring point. Eq. (59) is true providing that at the excitation point the rate of change of the phase is small and the propagating wave is dominating the response. Applying this equation for instance for $n = 2$, $L = 100$ m, $f = 102$ Hz and $c_g = 1300.15$ m/s from Fig. 7, results in a rate of change of the phase equal to -0.483 rad/Hz which matches with the results calculated from Fig. 11b.

Fig. 12(a and b) shows the tunnel radial displacement along its length. At frequency below the cut-on frequency where the response is dominated by the leaky waves, see also Fig. 7 (for $n = 2$), the curve has minima at 20.4, 48.25, 76 and 103.6 m, and hence with approximately 27.7 m periodicity. These are due to interference between leaky waves. For a displacement described by two leaky waves with complex

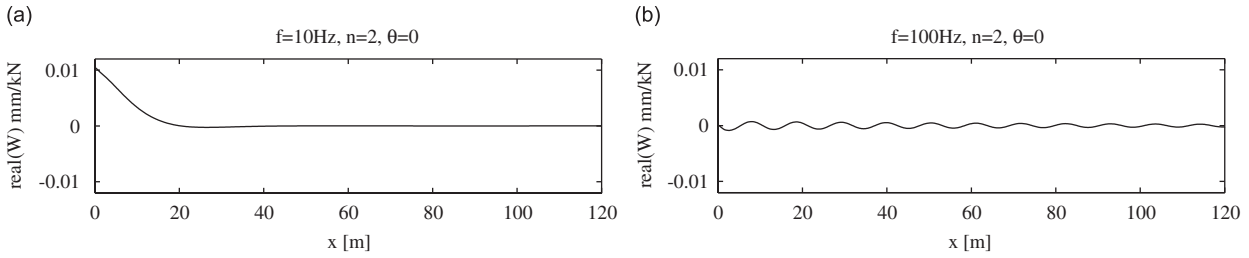

Fig. 13. The real part of the isolated thin shell response along the shell with $\theta = 0$ for a radial harmonic load applied at $x = 0$ with $n = 2$ and excitation frequency: (a) 10 Hz and (b) 100 Hz.

wavenumbers $\xi_1 = \gamma_1 + i\eta_1$ and $\xi_2 = \gamma_2 + i\eta_2$, the response y can be written as

$$y = c_1 e^{i(\gamma_1 + i\eta_1)x} + c_2 e^{i(\gamma_2 + i\eta_2)x}, \tag{60}$$

where c_1 and c_2 are the coefficients associated with each wave and can be complex quantities. Eq. (60) can be written in different form as

$$y = |c_1| e^{i(\gamma_1 + i\eta_1)x + i\phi_1} + |c_2| e^{i(\gamma_2 + i\eta_2)x + i\phi_2}, \tag{61}$$

where ϕ_1 and ϕ_2 are the phase of c_1 and c_2, respectively. Eq. (61) can be written as

$$y = |c_1| e^{-\eta_1 x}[\cos(\gamma_1 x + \phi_1) + i\,\sin(\gamma_1 x + \phi_1)] + |c_2| e^{-\eta_2 x}[\cos(\gamma_2 x + \phi_2) + i\,\sin(\gamma_2 x + \phi_2)]. \tag{62}$$

Multiplying by the conjugate and simplifying results in

$$y\,y^* = |y|^2 = |A_1|^2 e^{-2\eta_1 x} + |A_2|^2 e^{-2\eta_2 x} + 2|A_1|\,|A_2| e^{-(\eta_2 + \eta_2)x} \cos[(\gamma_1 - \gamma_2)x + \phi_1 - \phi_2]. \tag{63}$$

The oscillation in the previous equation arises from the cosine term with a period equal to $2\pi/(\gamma_1 - \gamma_2)$. From Fig. 7 and for $n = 2$, there are four leaky waves at $f = 10$ Hz with wavenumbers $\pm 0.113 + 0.133i$, $\pm 1.375 + 1.678i$. Leaky waves with wavenumbers $\pm 0.113 + 0.133i$ are dominating the response away from the load as those with wavenumbers $\pm 1.375 + 1.678i$ have higher decaying factors (due to the higher imaginary parts). Substituting $\gamma_1 = 0.113$ and $\gamma_2 = -0.113$, the oscillation period is 27.8 m, which agrees with the results in Fig. 12a.

The response at a frequency below the cut-on frequency decays rapidly compared with a frequency above the cut-on frequency. This can be confirmed by comparing Figs. 12a and 13b, and also by comparing Fig. 13a and b, which show the real part of the response at frequencies of 10 and 100 Hz, i.e. below and above the cut-on frequency. The wavelength in Fig. 13b is 10.58 m; equal to wavenumber 0.59 rad/m which matches with the propagating wavenumber for $f = 100$ Hz, $n = 2$ in Fig. 7.

7. The surrounding soil modelled as an elastic continuum

The free-vibration equation of a full-space with a cylindrical cavity is calculated by the following equation (see Eq. (40) of Ref. [9])

$$\mathbf{T}_m \mathbf{B} = [\mathbf{T}_\infty]_{r=a} \mathbf{B} = Z(3,1), \tag{64}$$

where $Z(3,1)$ is a 3×1 vector with zero elements, $\mathbf{T}_m = [\mathbf{T}_{1\infty}]_{r=a}$ for the first loading combination and $\mathbf{T}_m = [\mathbf{T}_{2\infty}]_{r=a}$ for the second loading combination. The elements of $[\mathbf{T}_{2\infty}]_{r=a}$ can be calculated from the following relationship (see Eq. (A.2)):

$$[\mathbf{T}_{\infty 2}] = \begin{bmatrix} 1 & -1 & -1 \\ -1 & 1 & 1 \\ 1 & -1 & -1 \end{bmatrix} * [\mathbf{T}_{\infty 1}]. \tag{65}$$

Using the same argument which leads to Eq. (56), one can prove that $|[\mathbf{T}_{1\infty}]_{r=a}| = -|[\mathbf{T}_{2\infty}]_{r=a}|$. Equating these determinants to zero, both matrices lead to the same dispersion equation. Two main characteristics are associated with the current problem:

- the dispersion equation is not in polynomial form but it comprises of the modified Bessel function of the second kind and hence a different numerical method should be used to calculate the roots;
- unlike thin cylindrical shells in the previous section, the forced vibration solution does not consists only of the normal wave solutions (propagating, evanescent and leaky waves), but additional solutions arise due to the integration along the branch cuts. Note that due to the terms $\alpha = \sqrt{\xi^2 - \omega^2/c_1^2}$ and $\beta = \sqrt{\xi^2 - \omega^2/c_2^2}$ that come in the elements of $\mathbf{T}_m$, branch points occur at $\xi = \pm\xi_c$ and $\xi = \pm\xi_s$, where $\xi_c = \omega/c_1$ is the wavenumber of the compression wave and $\xi_s = \omega/c_2$ is the wavenumber of the shear wave.

In this section, only the real solutions of the dispersion equation are searched. Newton–Raphson method in Ref. [30] is used to find the roots of the dispersion equation. At a given frequency and cross-sectional wavenumber n, the iterative formula for Newton–Raphson reads

$$\xi_{j+1} = \xi_j + \Delta \text{ with } \Delta = -D(\xi_j)/D'(\xi_j), \tag{66}$$

where $D(\xi_j)$ is the dispersion equation calculated at ξ_j and $D'(\xi_j)$ is the derivative of the dispersion equation evaluated at ξ_j. The iteration in Eq. (66) converges if the starting guess ξ_1 lies near a root. The derivative is calculated using the following relationship [31]:

$$\begin{aligned}\frac{d}{d\xi}\left|\mathbf{T}_m(\xi)\right| &= \frac{d}{d\xi}\left|\mathbf{T}_m(1), \mathbf{T}_m(2), \mathbf{T}_m(3)\right| \\ &= \left|\dot{\mathbf{T}}_m(1), \mathbf{T}_m(2), \mathbf{T}_m(3)\right| + \left|\mathbf{T}_m(1), \dot{\mathbf{T}}_m(2), \mathbf{T}_m(3)\right| + \left|\mathbf{T}_m(1), \mathbf{T}_m(2), \dot{\mathbf{T}}_m(3)\right|,\end{aligned} \tag{67}$$

where $\mathbf{T}_m(1)$,$\mathbf{T}_m(2)$,$\mathbf{T}_m(3)$ are the columns of matrix $\mathbf{T}_m$ and $\dot{\mathbf{T}}_m(j)$ is a column vector which contains the first derivative of the elements of $\mathbf{T}_m(j)$. The advantage of Eq. (67) is that only closed-form expressions are required for derivatives of individual elements rather than calculating a closed-form expression of the determinant and then differentiating term by term.

It is found that at a given frequency, the dispersion equation satisfies $|\mathbf{T}_m(-\xi)| = |\mathbf{T}_m(\xi)|$ and $|\mathbf{T}_m(\xi^*)| = |\mathbf{T}_m(\xi)|^*$. Hence, if ξ is a root, then $-\xi$ and ξ^* are also roots. Thus, for real roots, only positive values are searched.

A Matlab [24] code is written to calculate the real positive roots of the dispersion equation. To decrease the running time, the use of "for loops" is minimised. At a given frequency, a vector of M values of ξ is used; each element represents a starting point. Two Matlab functions are coded to calculate the dispersion equation and its derivative, which result into two vectors with M elements. Instead of calculating a 3×3 matrix for each point of the vector and then calculating the determinant, the vector is processed at once. The dispersion-equation function calculates nine vectors (each with M elements) corresponding to the elements of $\mathbf{T}_m$, and the determinant is calculated at once using a closed-form expression for the determinant of a 3×3 matrix. Similarly, the dispersion-equation-derivative function calculates additional nine vectors corresponding to the elements of the matrix derivative in Eq. (67). After some iterations, the elements of the vector from the last iteration are compared with those from the iteration before. Those elements which have converged are taken as solutions of the dispersion equation.

Fig. 14a shows the dispersion curves of the soil with a cylindrical cavity for the parameters given in Table 1. In the frequency range of interest, waves with cross-sectional wavenumbers n from 0 to 5 can propagate freely with phase velocities in the range between the shear wave velocity and the Rayleigh wave velocity. For each cross-sectional wavenumber n, waves have cut-on frequencies at velocity equal to the shear wave velocity. By increasing the frequencies, the phase velocity of the propagating waves decreases and approaches the Rayleigh wave velocity. This is expected because the wavelength of the propagating wave at high frequency is small compared to the cavity diameter. Hence, the cavity behaves as a free-surface equivalent to the free surface of a half-space. Fig. 14b shows the phase velocities of the propagating waves. The Rayleigh wave velocity is

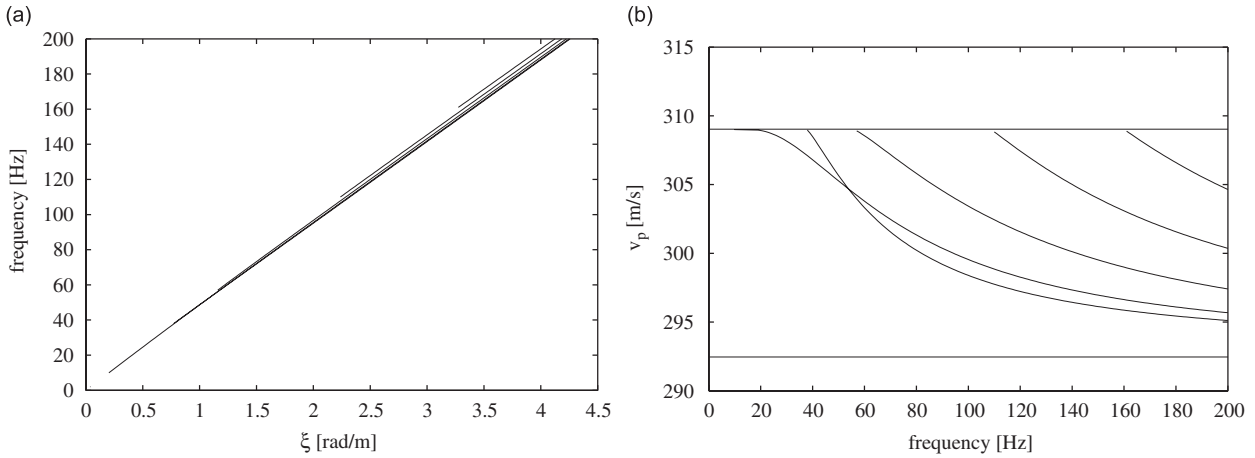

Fig. 14. (a) Dispersion curves of the given soil modelled as a full-space with cylindrical cavity. (b) The phase velocity of the dispersion curves.

Table 2
Cut-on frequencies of the soil model

n	f_n (Hz)
0	37.5
1	9.93
2	55.52
3	108.57
4	159.89

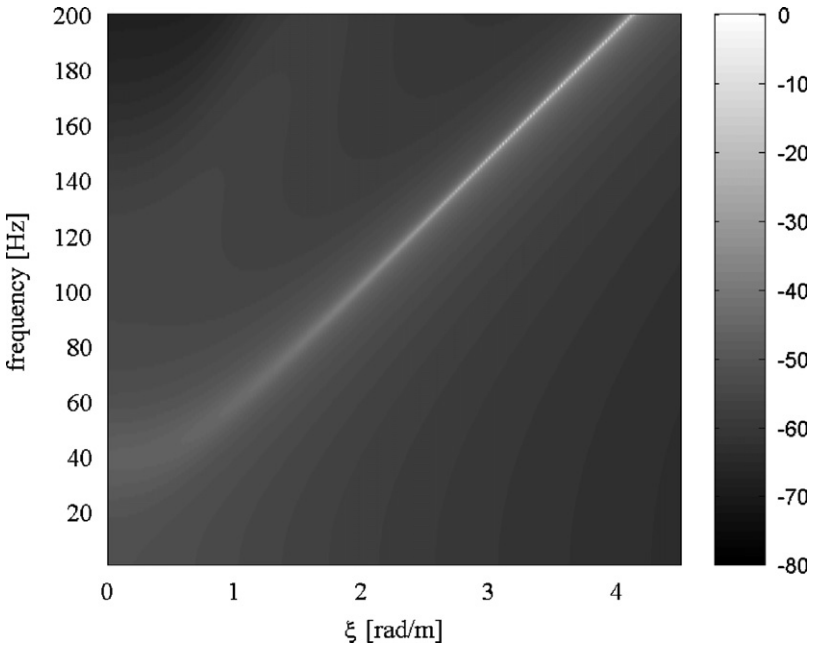

Fig. 15. FRF of the soil model for $n = 4$ calculated at the cavity surface.

calculated by Ref. [25] as

$$c_3 = c_2(0.87 + 1.12v)/(1 + v). \tag{68}$$

It can be seen from Fig. 14b that there is a cut-on frequency for each cross-sectional wavenumber. The cut-on frequencies are given in Table 2. The results given in this section are compared with the results of Bostrom and Burden [32]. They present a study on propagation of surface waves along a cylindrical cavity. They calculate the displacement in terms of the transverse (SH and SV) and compression components. The dispersion equation is derived in a closed form. Using the limiting forms of the modified Bessel functions, two simplified equations are presented to calculate the cut-on frequencies; an equation for $n = 0$ and another equation for $n \geqslant 2$. These equations are used by the authors to recalculate the cut-on frequencies using the soil parameters in Table 1. Identical results are obtained for $n = 0,2,3,4$. However, Bostrom and Burden claim that there is no cut-on frequency for $n = 1$, which does not agree with the result of this work. To check this, the dispersion equation derived by Bostrom and Burden is investigated for $n = 1$ and it is found that it has a cut-on frequency at the same value given in Table 2.

Fig. 15 shows the displacement FRF for $n = 4$ calculated at the cavity surface. The sharp curve follows the dispersion curve for $n = 4$ in Fig. 14a for frequencies from 200 Hz down to the cut-on frequency. The peaks continue below the cut-on frequency until it gets to $\xi = 0$ at about $f = 40$ Hz. Above the cut-on frequency, the sharp curve has infinite values that are attributed to zero values of the dispersion equation. However, peaks below the cut-on frequency have finite values and are attributed to maximal values of the FRF (for the forced vibration).

8. The PiP model

From Eq. (41) of Ref. [9], one can write the dispersion equation of the PiP model in the following form:

$$|\mathbf{A}_E\mathbf{U}_m + \mathbf{T}_m| = 0, \tag{69}$$

with $\mathbf{U}_m = [\mathbf{U}_\infty]_{r=a}$ and $\mathbf{T}_m = [\mathbf{T}_\infty]_{r=a}$.

As same as the dispersion equation of the thin shell model and the soil model, the dispersion equation of the PiP model is independent of the loading combination and this has been confirmed by comparing the dispersion equations resulting from both of the loading combinations.

Newton–Raphson method is used again for this case to calculate the solutions of the dispersion equation. No real roots are found for the parameters given in Table 1 in the frequency range of interest. This means that besides its importance in supporting the soil, the tunnel wall does not allow waves to propagate freely.

Figs. 16 and 17 show the PiP model response for a radial input and tangential input, respectively, for a frequency of 30 Hz and for cross-sectional wavenumbers $n = 0,1$. The results in Fig. 16 are calculated using $\tilde{q}_x = 0$, $\tilde{q}_\theta = 0$ and $\tilde{q}_r = 1$, and the formulation for the first loading combination. The results in Fig. 17 are calculated using Eqs. (50) and (51), substituting $\tilde{q}_x = 0$, $\tilde{q}_\theta = 1$ and $\tilde{q}_r = 0$, and the formulation for the second loading combination. For $n = 0$, the PiP model has no tangential response for the radial input and vice versa, i.e. $H_{WV} = H_{VW} = 0$. Moreover, because of reciprocity [33], the relationship $H_{WV} = H_{VW}$ holds for any value of n at the tunnel–soil interface (compare H_{VW} for $r = 3$ m in Fig. 16c with H_{WV} for $r = 3$ m in 17a).

Near and at the tunnel–soil interface, the response is distributed over a wide range of wavenumbers, while away from the tunnel the response is confined to a narrow band of wavenumbers. Three regions of response are identified according to values of wavenumber: values of wavenumber less than the compression wavenumber; values of wavenumber greater than the compression wavenumber but less than the shear wavenumber; and values greater than the shear wavenumber. In the first region, both compression and shear waves propagate. In the second, only shear waves propagate and in the third both compression and shear waves are attenuated. For the results in Figs. 16 and 17, the compression wavenumber is $\omega/c_p = 0.2$ rad/m and the shear wavenumber is $\omega/c_s = 0.61$ rad/m and it can be seen than wavenumbers greater than 0.61 are greatly attenuated with distance away from the source. The problem of plane wave propagation and attenuation in 3D elastic space is analogous to the problem of pressure wave propagation in fluid due to a travelling wave in a plate, see Ref. [34] for example.

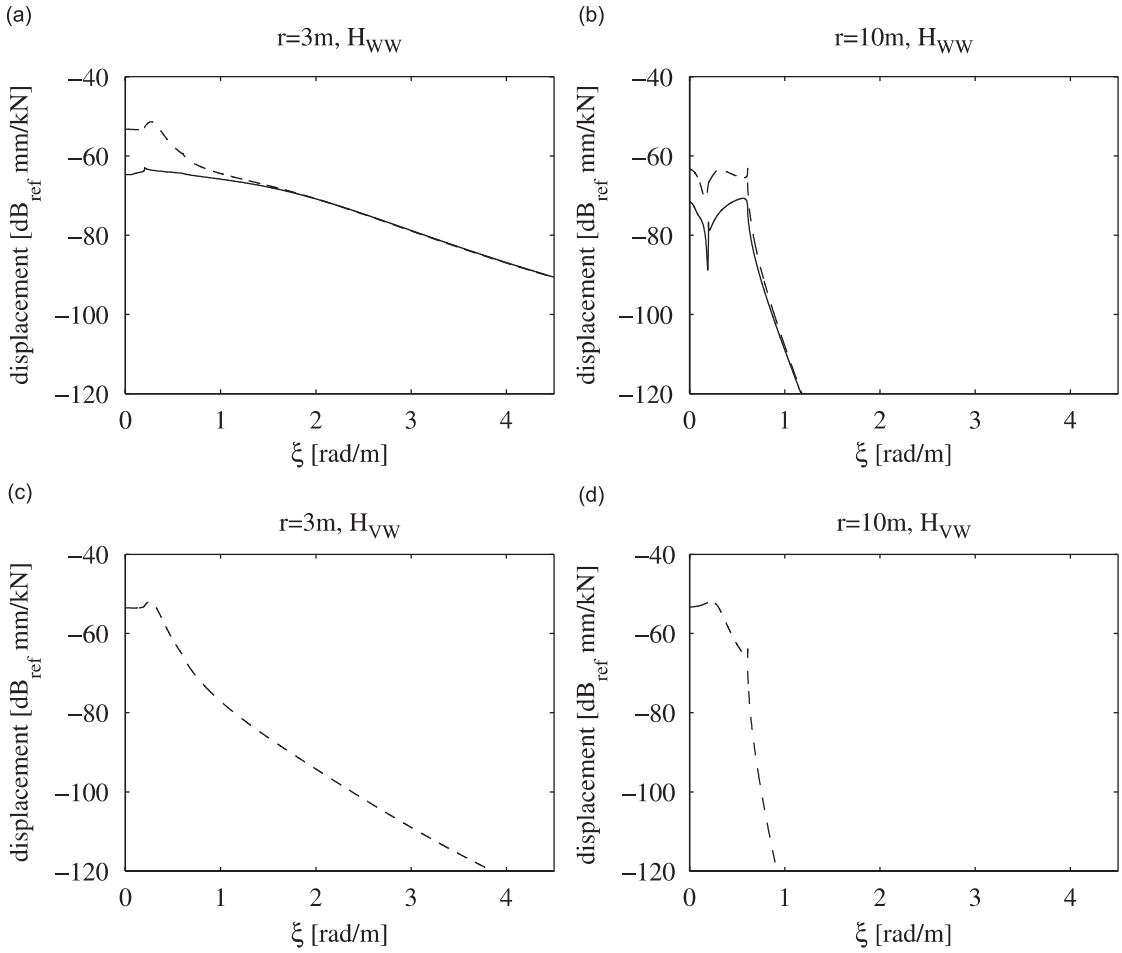

Fig. 16. FRF of the PiP model for $n=0$ (-) and $n=1$ (- -) for a radial input on the inner surface of the tunnel. H_{WV} is the radial displacement FRF (equivalent to $\tilde{u}_r(n,\xi,\omega=2\pi\times 30\,\mathrm{rad/s})$) due to a radial input while H_{VV} is the tangential displacement FRF (equivalent to $\tilde{u}_\theta(n,\xi,\omega=2\pi\times 30\,\mathrm{rad/s})$) due to a radial input. The tunnel–soil interface lies at $r=3$.

The wave propagation study in this paper has addressed the PiP model so far. In the next section, the dispersion equations of tracks on rigid foundations will be investigated. When the stiffness of track's support, i.e. the slab bearings, is much smaller that the stiffness of the PiP model, it is possible to calculate the forces generated on the tunnel wall due to any loading on the rails from a model of a track coupled to a rigid tunnel wall, i.e. a track on rigid foundation. These forces can then be used as input to the PiP model to calculate the vibration levels around the tunnel. Such a procedure may be accurate but it will not be used in this paper, as the direct formulation in Section 2 does not take long time to be performed. However, attention should be drawn to the importance of dispersion curves of a track on a rigid foundation in which force magnification happens. This will be discussed in the next section.

8.1. Dispersion characteristics of the track

Fig. 18 shows a floating-slab track attached to a rigid foundation via two lines of support. The track has five degrees of freedom. The force–displacement relationship is calculated by the following equation:

$$\tilde{\mathbf{F}}=[\tilde{\mathbf{K}}]\tilde{\mathbf{y}}, \tag{70}$$

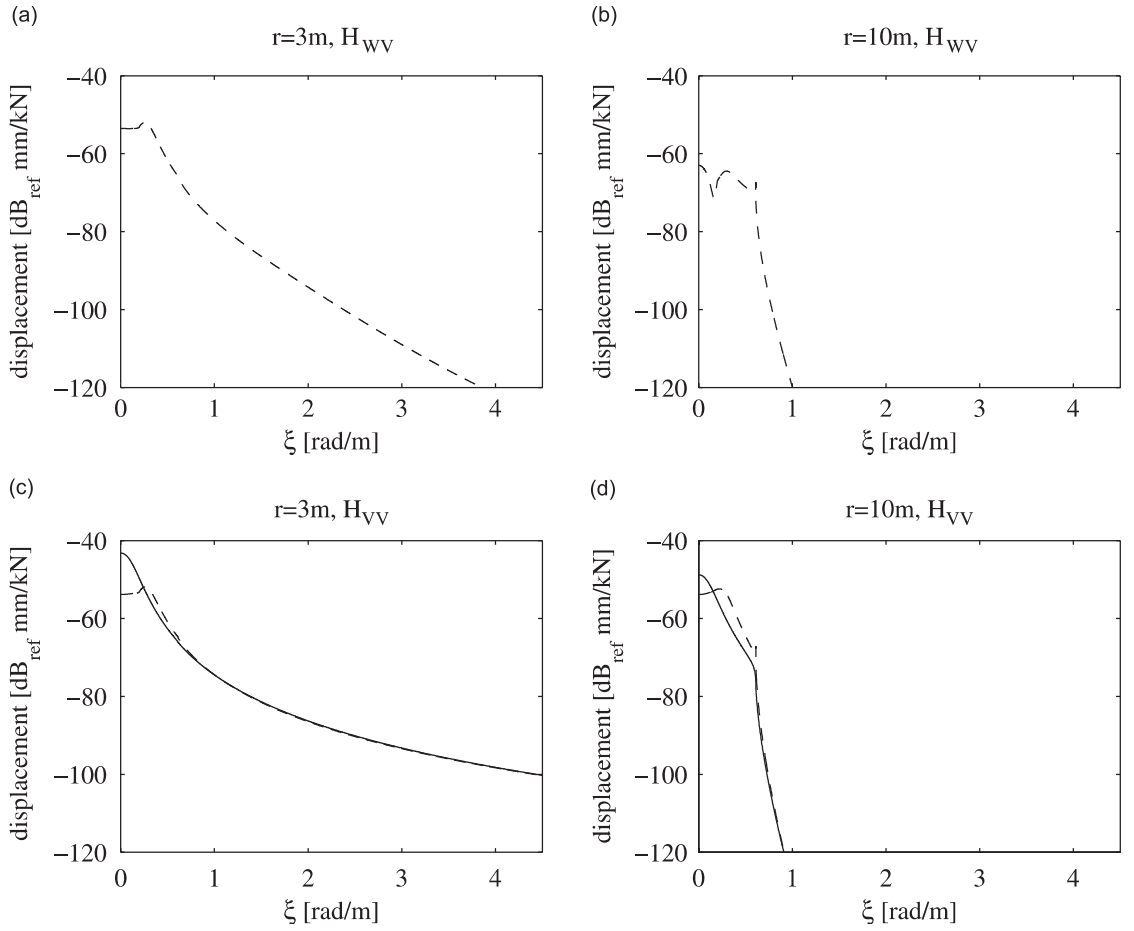

Fig. 17. FRF of the PiP model for $n = 0$ (-) and $n = 1$ (- -) for a tangential input on the inner surface of the tunnel. H_{WV} is the radial displacement FRF (equivalent to $\tilde{u}_r(n, \xi, \omega = 2\pi \times 30\,\mathrm{rad/s})$) due to a tangential input while H_{VV} is the tangential displacement FRF (equivalent to $\tilde{u}_\theta(n, \xi, \omega = 2\pi \times 30\,\mathrm{rad/s})$) due to a tangential input. The tunnel–soil interface lies at $r = 3$.

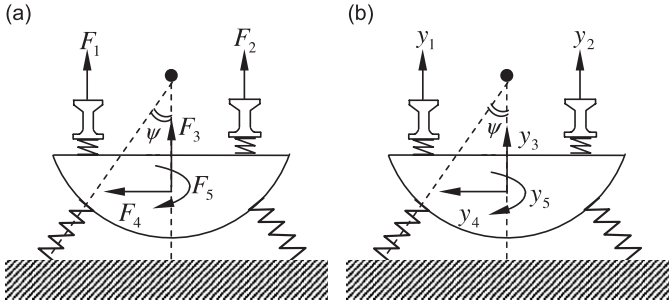

Fig. 18. Floating-slab track on rigid bed: (a) forces and (b) displacements.

where $\tilde{\mathbf{F}} = [\tilde{F}_1, \tilde{F}_2, \tilde{F}_3, \tilde{F}_4, \tilde{F}_5]^{\mathrm{T}}$, $\tilde{\mathbf{y}} = [\tilde{y}_1, \tilde{y}_2, \tilde{y}_3, \tilde{y}_4, \tilde{y}_5]^{\mathrm{T}}$,

$$\tilde{\mathbf{K}} = \begin{bmatrix} \tilde{K}_r + k_r & 0 & -k_r & 0 & -k_r \cdot a_t \\ 0 & \tilde{K}_r + k_r & -k_r & 0 & k_r \cdot a_t \\ -k_r & -kr & \tilde{K}_v + 2k_r + 2k_n c^2 + 2k_s s^2 & 0 & 0 \\ 0 & 0 & 0 & \tilde{K}_h + 2k_n s^2 + 2k_s c^2 & -2k_n(r_t - b_b)s^2 + 2k_s c[r_t - (r_t - b_b)c] \\ -k_r a_t & k_r a_t & 0 & -2k_n(r_t - b_b)s^2 + 2k_s c[r_t - (r_t - b_b)c] & \tilde{K}_\gamma + 2k_s[r_t - (r_t - b_b)c]^2 + 2k_r a_t^2 + 2k_n(r_t - b_b)^2 s^2 \end{bmatrix},$$

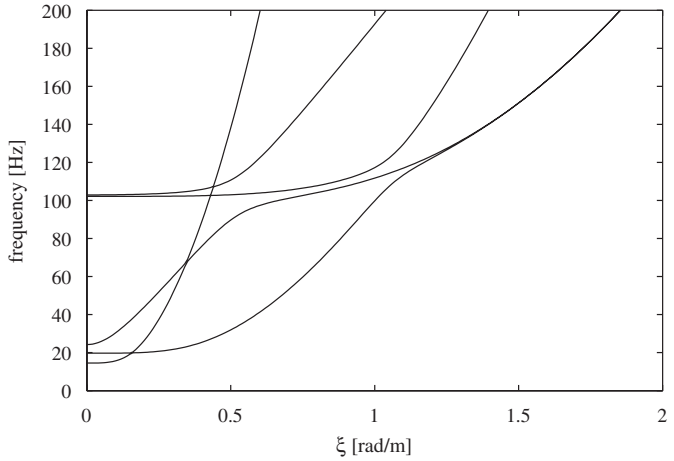

Fig. 19. Dispersion curves for the chosen floating-slab track on rigid bed.

Table 3
Cut-on frequencies and mode shapes for a track on rigid bed

Mode	1	2	3	4	5
Cut-on frequency (Hz)	14.50	19.71	24.20	102.14	102.92
$\tilde{y}_1$	0.02	1.00	0.80	1.00	1.00
$\tilde{y}_2$	−0.02	1.00	−0.80	1.00	−1.00
$\tilde{y}_3$	0.00	0.96	0.00	−0.03	0.00
$\tilde{y}_4$	1.00	0.00	−0.11	0.00	0.00
$\tilde{y}_5$	0.27	0.00	1.00	0.00	−0.06

$\tilde{K}_r = 1/\tilde{H}_r = EI_r\xi^4 - m_r\omega^2$, $\tilde{K}_v = 1/\tilde{H}_v = EI_v\xi^4 - m_s\omega^2$, $\tilde{K}_h = 1/\tilde{H}_h = EI_h\xi^4 - m_s\omega^2$, $\tilde{K}_\gamma = 1/\tilde{H}_\gamma = GK\xi^2 - J\omega^2$, $c = \cos\psi$, $s = \sin\psi$, EI_h is the bending stiffness of the slab in the horizontal direction and all the other parameters are defined in Section 2.

The stiffness matrix $\tilde{\mathbf{K}}$ in Eq. (70) is assembled using the direct stiffness method which is usually used to calculate stiffness matrices for structures under static loads [35]. Alternatively, the stiffness matrix can be calculated by using the formulation in Section 2.1 and setting the FRFs of the PiP model to zero.

To calculate the dispersion equation, the determinant of $\tilde{\mathbf{K}}$ is set to zero. Again, only real roots are searched. The Matlab function "roots" is used to calculate the solutions. Fig. 19 shows the dispersion curves of a 20 Hz floating-slab track for the frequency range 0–200 Hz and using the track parameters given in Table 1 with $\psi = 15^\circ$. Table 3 shows the cut-on frequencies of this track along with the propagating modes (the eigenvectors) at the cut-on frequencies.

The modes from the first to the fifth are called: the horizontal-slab mode, the vertical-slab mode, the torsional-slab mode, the in-phase-rails mode and the out-of-phase-rails mode, respectively. The horizontal-slab mode has rails' displacements and rotational displacement of the slab, which vanish if $\psi = 0$.

Two cases are of significant importance. The first is when $\tilde{F}_1 = \tilde{F}_2$. In this case, only two modes can propagate; these are the second and the fourth modes. The second case is when $\tilde{F}_1 = -\tilde{F}_2$. This time three modes can propagate; the first, the third and the fifth. Calculating the dispersion curves for the full track model (consisting of the track and the PiP model) is complicated. However, the dispersion curves of the track on a rigid bed are important and help identifying the peaks of the FRFs of the full track–tunnel–soil model.

8.2. Results of the full model

Fig. 20 shows the normal force of the left slab bearing calculated by the full track model as described in Section 2.1 (Fig. 2) and by the rigid-bed model (Fig. 18) as calculated by Eq. (70). The results are for applied

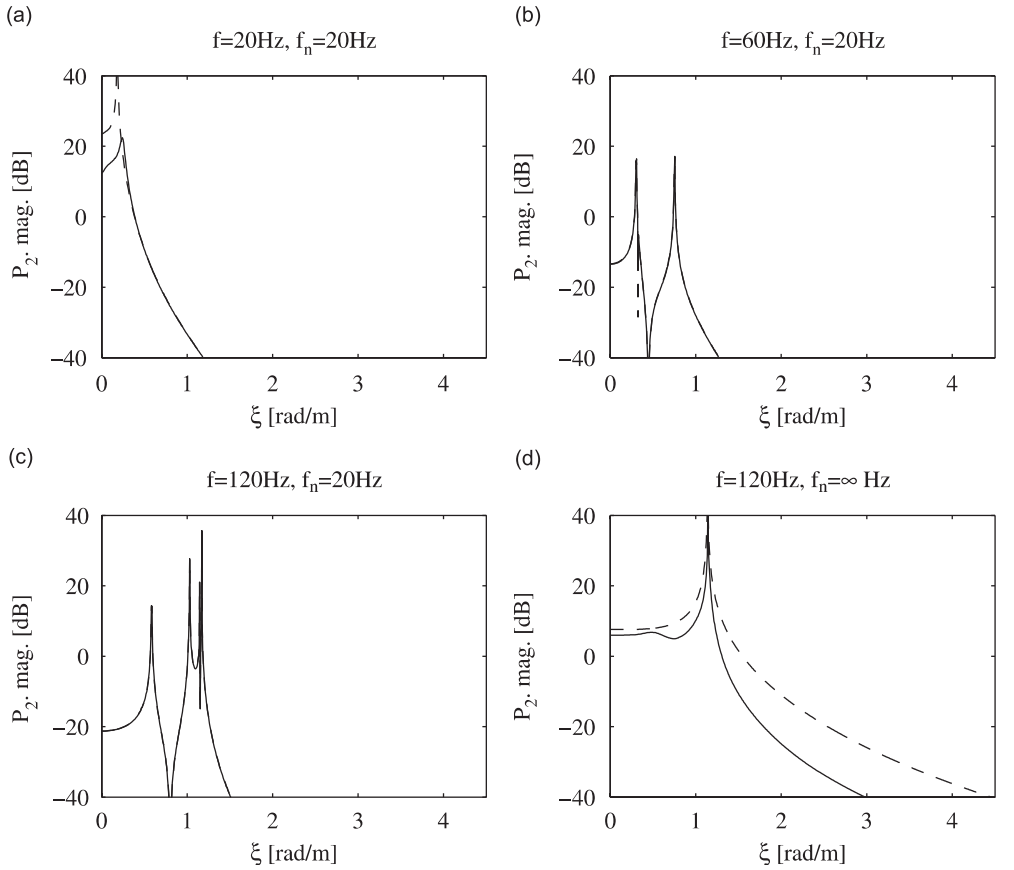

Fig. 20. $\tilde{P}_2$ calculated by the full track model (-) and the rigid-bed model (- -) for loading $\tilde{F}_1 = 1$, $\tilde{F}_2 = 0$, for different excitation frequencies and different slabs: (a) $f = 20$ Hz, $f_n = 20$ Hz; (b) $f = 60$ Hz, $f_n = 20$ Hz; (c) $f = 120$ Hz, $f_n = 20$ Hz; and (d) $f = 120$ Hz, $f_n = \infty$ Hz.

forces $\tilde{F}_1 = 1$ and $\tilde{F}_2 = 0$ with $\psi = 15^\circ$ and $\Re = 0.5$. Fig. 20(a–c) are calculated for a 20 Hz slab with excitation frequencies 20, 60 and 120 Hz, respectively, while a directly-fixed slab (∞ Hz) with 120 Hz excitation frequency is used to produce the results in Fig. 20d.

It can be seen that the forces on the tunnel invert can be calculated approximately using the rigid-bed model. The accuracy of this approximation decreases at frequencies and wavenumbers on the track dispersion curves (Fig. 20a) and also decreases by increasing the stiffness of the slab bearings (Fig. 20d). Note that peaks occur at wavenumbers defined by the dispersion curves of the track on rigid bed, this is confirmed by comparing the wavenumbers in which peaks occur in a, b and c with the corresponding wavenumbers as plotted in Fig. 19. These peaks appear in the displacement FRF of the soil as in Fig. 21 which shows the soil displacement FRFs at angle $\theta = 120^\circ$ and 10 m away from the tunnel centre for $\tilde{F}_1 = 1$, $\tilde{F}_2 = 0$, $\psi = 15^\circ$, $\Re = 0.5$, $f_n = 20$ and 60 Hz excitation frequency. The number of collocation points for the uniform support is taken as $M = 10$ which is found to be accurate for the current parameters. Note that some modes have little contribution to the response and hence no pronounced peaks are observed at their eigen frequencies.

Figs. 22 and 23 show the space–domain radial displacement at the far field at $x = 0$, $\theta = 120$ and $r = 30$ m for two loading combinations (a) $F_1 = 1$, $F_2 = 1$; and (b) $F_1 = 1$, $F_2 = -1$. Results are transformed from the wavenumber domain using the discrete inverse Fourier transform with spatial interval $\mathrm{d}x = 0.25$ m and number of points $N = 2^{14}$. Loss factors of 2% for rails in bending, 5% for slab in bending and torsion and 10% for railpads and slab bearings, 3% for the tunnel and 6% for the soil are introduced to account for damping. The results in Fig. 22 are for directly-fixed slab, modelled by using a high value of slab natural frequency, $f_n = 1000$ Hz. The results in Fig. 23 are for 10 Hz floating slab. The results show clear undulation

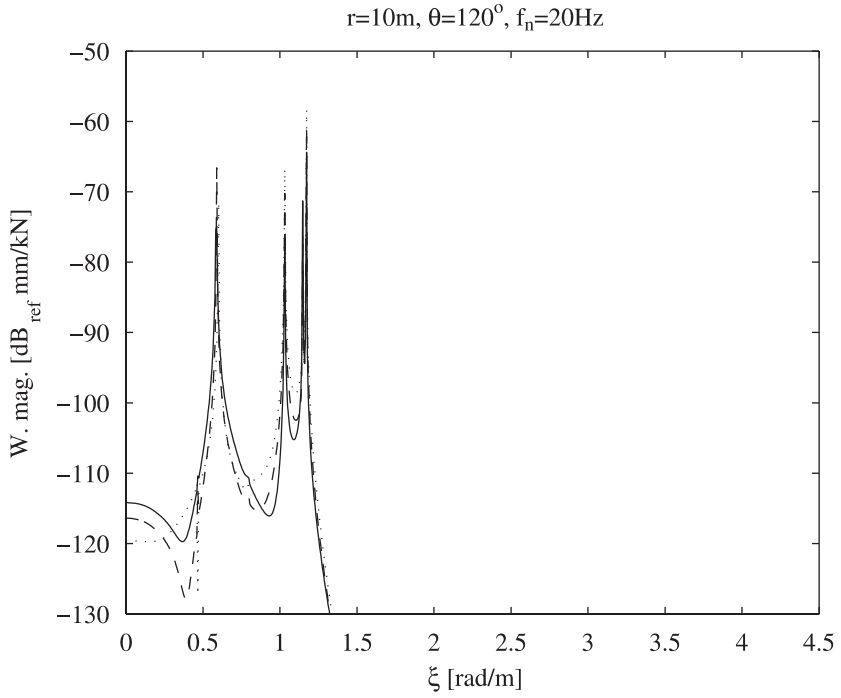

Fig. 21. The radial displacement calculated at $r = 10\,\text{m}$ and $\theta = 120^\circ$ for the track supported on: two lines of support (-), three lines of support (- -) and uniform support (..). The loads are $\tilde{F}_1 = 1$, $\tilde{F}_2 = 0$ with 120 Hz excitation frequency.

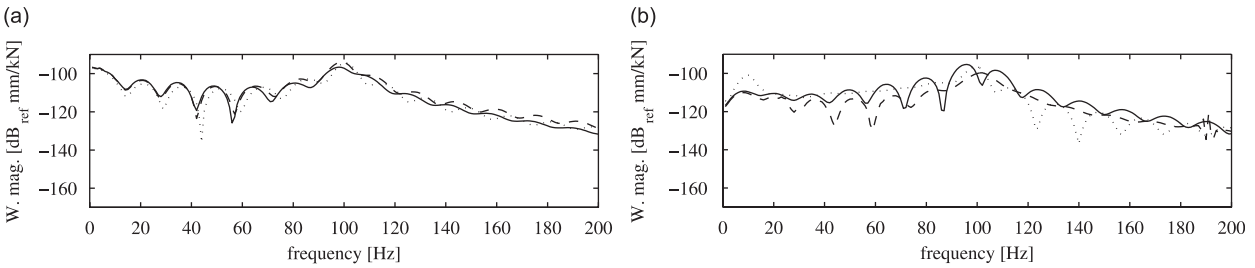

Fig. 22. The radial displacement calculated at $x = 0$, $r = 30\,\text{m}$ and $\theta = 120^\circ$ for a track with $f_n = \infty$ supported on: (-) two lines of support, (- -) three lines of support and (..) uniform support. The loads are (a) $F_1 = 1$, $F_2 = 1$ and (b) $F_1 = 1$, $F_2 = -1$ applied at the rails at $x = 0$.

with step of about 15 Hz between troughs. This is attributed to interference between shear and compression waves in the soil. It is illustrated in Ref. [11] that undulation is expected with a step of $c_p c_s/[r(c_p - c_s)]$ Hz when measuring the response at a distance r away from a point source which sends both compression wave and shear wave with velocities c_p, c_s, respectively. Using the wave velocities of the soil in Table 1 with a distance $r = 31.6\,\text{m}$, results in a step of approximately 15 Hz. The undulation is clearer and more regular in Fig. 22 than in Fig. 23. This is because the slab is strongly coupled to the tunnel in the first case and therefore the energy has no way to go but to the soil, hence it is more analogous to the case of a point source. For the 10 Hz floating slab, part of the energy propagates along the track before going into the soil. The curves in Fig. 23a resonate at frequency slightly less than the natural frequency of the slab. This is because the tunnel wall adds some stiffness in series to the stiffness of the slab bearings which brings the natural frequency down. The resonant frequencies in Fig. 23b occur at the torsion natural frequency of the slab below 20 Hz. Note the slab supported via two lines has the largest torsional resonant frequency as more stiffness of the support is kept away from the slab centre. Therefore, this slab is less efficient in isolating vibration from torsional inputs as can be seen from its performance at high frequencies, above 100 Hz.

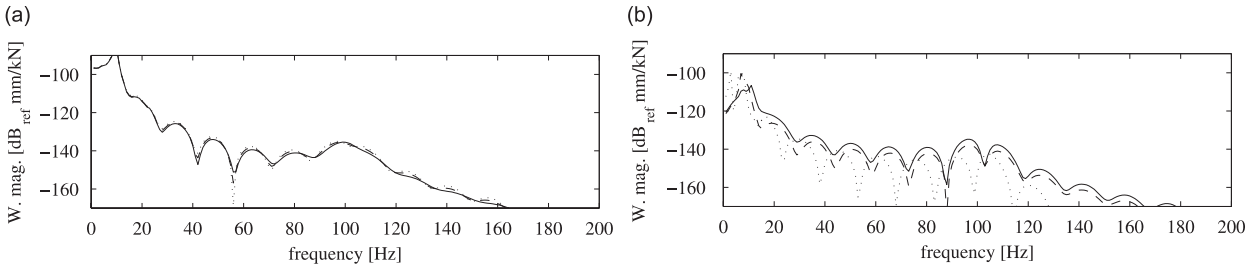

Fig. 23. The radial displacement calculated at $x = 0$, $r = 30\,\text{m}$ and $\theta = 120^\circ$ for a track with $f_n = 10\,\text{Hz}$ supported on: (-) two lines of support, (- -) three lines of support and (..) uniform support. The loads are (a) $F_1 = 1$, $F_2 = 1$ and (b) $F_1 = 1$, $F_2 = -1$ applied at the rails at $x = 0$.

Fig. 22a shows that modelling the directly-fixed slab using two lines of supports results in about $\pm 4\,\text{dB}$ difference compared to the most realistic model, i.e. the uniform support in the frequency range of interest. As the case of two lines of supports is more computationally efficient, such a model can be preferable to calculate the far-field vibration. Note that as the stiffness of the slab bearings decreases, all models result in the same far-field vibration as can be seen from Fig. 23a. For the far-field calculations, the distribution of supports has more significant effect on the slab dynamics than on the slab–tunnel interaction. The slab–tunnel interaction refers here to the tendency of the slab to propagate more or less vibration as a result of exciting certain circumferential modes n of the PiP model. It can be seen from Figs. 22a and 23a that the far-field vibration from different distribution differs by a maximum of $\pm 4\,\text{dB}$. This is because all slabs have the same dynamics in bending for these two figures and the applied forces are set to produce the bending effect. The noticeable differences between the curves in Figs. 22b and 23b are due to the differences in the natural frequencies of the torsion mode and the horizontal mode of the slab that arise from different distribution of slab bearings.

9. Conclusions

In this paper, a formulation for a full model of a track in an underground railway tunnel is presented. The model comprises of a floating-slab track coupled via slab bearings to the PiP model which accounts for a tunnel wall and its surrounding soil. Special attention is given to the slab support: slabs are attached to the tunnel wall in one of three ways; via two lines, three lines or a uniform support. An important aspect of the uniform support is that it allows modelling of a directly-fixed slab by setting the support stiffness to infinity.

Wave propagation in the PiP model and its separate components is investigated. The dispersion curves for a tunnel wall modelled as a thin shell are compared with a tunnel modelled as a thick shell (using the elastic continuum theory) and a good agreement is obtained in the frequency range 0–200 Hz. For the soil with a cylindrical cavity, waves propagate near the surface with velocities between the Rayleigh wave velocity and the shear wave velocity. At high frequencies, these waves behave as surface waves in a half-space. The results calculated for the soil are compared with published results in the context of wave propagation.

Waves can propagate in a free tunnel wall and in a full-space with a cylindrical cavity, but due to coupling there is no free wave propagation in the PiP model for the parameters of the tunnel and soil considered here. The soil acts as a filter that attenuates plane waves with wavenumbers larger than the shear wavenumber in a full-space and propagates the other wavenumbers.

The dispersion curves of a floating-slab track on rigid foundation are also calculated. These curves have a great effect on the FRFs of the full track–tunnel–soil system. The generated forces on the tunnel exhibit peaks at wavenumbers and frequencies along these curves. It is shown that for the purpose of far-field calculations, the distribution of supports has more effect on the track dynamics rather than the track–tunnel interaction. A simple model of the support such as the two line support in this paper can be sufficient to calculate vibration in the far-field without losing accuracy lost even when modelling a directly-fixed slab. However, suitable values for the horizontal and vertical stiffness and the angle of distribution of bearings should be used that result in the required natural frequencies of the slab track.

Appendix A. Transfer matrices for the second loading combination

The PiP model is used in this paper to model a tunnel wall and the surrounding soil. A detailed derivation of the response of this model to a symmetrical loading combination (called here the first loading combination) is presented by Forrest and Hunt [9]. The first loading combination involves cosine terms with stresses and displacements in the radial and longitudinal directions of the tunnel and sine terms in the tangential direct, see Eqs. (4) and (5) of Ref. [9] for instance. A similar procedure is followed in this work to derive transfer matrices of the PiP model for the second loading combination. This is done by replacing every cosine by a sine and vice versa. In this paper, subscript 1 is used with transfer matrices of the first loading combination such as $\mathbf{A}_1$. Subscript 2 is used with transfer matrices of the second loading combination such as $\mathbf{A}_2$. Note that Forrest and Hunt use no subscripts at all, as they only consider the first combination.

For the thin shell, the relationship between the transfer matrix of the second loading combination and that of the first loading combination is given by

$$\mathbf{A}_2 = \begin{bmatrix} \mathbf{A}_1(1,1) & -\mathbf{A}_1(1,2) & \mathbf{A}_1(1,3) \\ -\mathbf{A}_1(2,1) & \mathbf{A}_1(2,2) & -\mathbf{A}_1(2,3) \\ \mathbf{A}_1(3,1) & -\mathbf{A}_1(3,2) & \mathbf{A}_1(3,3) \end{bmatrix}. \tag{A.1}$$

The expressions for $\mathbf{A}_1(1,1)$, $\mathbf{A}_1(1,2)$, etc. are given in pp. 700–701 of Ref. [9].

For the elastic continuum, the relationship between the transfer matrices of the second loading combination and these of the first loading combination are given by

$$\mathbf{T}_2 = \begin{bmatrix} \mathbf{T}_1(1,1) & \mathbf{T}_1(1,2) & -\mathbf{T}_1(1,3) & -\mathbf{T}_1(1,4) & -\mathbf{T}_1(1,5) & -\mathbf{T}_1(1,6) \\ -\mathbf{T}_1(2,1) & -\mathbf{T}_1(2,2) & \mathbf{T}_1(2,3) & \mathbf{T}_1(2,4) & \mathbf{T}_1(2,5) & \mathbf{T}_1(2,6) \\ \mathbf{T}_1(3,1) & \mathbf{T}_1(3,2) & -\mathbf{T}_1(3,3) & -\mathbf{T}_1(3,4) & -\mathbf{T}_1(3,5) & -\mathbf{T}_1(3,6) \\ \mathbf{T}_1(4,1) & \mathbf{T}_1(4,2) & -\mathbf{T}_1(4,3) & -\mathbf{T}_1(4,4) & -\mathbf{T}_1(4,5) & -\mathbf{T}_1(4,6) \\ -\mathbf{T}_1(5,1) & -\mathbf{T}_1(5,2) & \mathbf{T}_1(5,3) & \mathbf{T}_1(5,4) & \mathbf{T}_1(5,5) & \mathbf{T}_1(5,6) \\ \mathbf{T}_1(6,1) & \mathbf{T}_1(6,2) & -\mathbf{T}_1(6,3) & -\mathbf{T}_1(6,4) & -\mathbf{T}_1(6,5) & -\mathbf{T}_1(6,6) \end{bmatrix} \tag{A.2}$$

and

$$\mathbf{U}_2 = \begin{bmatrix} \mathbf{U}_1(1,1) & \mathbf{U}_1(1,2) & -\mathbf{U}_1(1,3) & -\mathbf{U}_1(1,4) & -\mathbf{U}_1(1,5) & -\mathbf{U}_1(1,6) \\ -\mathbf{U}_1(2,1) & -\mathbf{U}_1(2,2) & \mathbf{U}_1(2,3) & \mathbf{U}_1(2,4) & \mathbf{U}_1(2,5) & \mathbf{U}_1(2,6) \\ \mathbf{U}_1(3,1) & \mathbf{U}_1(3,2) & -\mathbf{U}_1(3,3) & -\mathbf{U}_1(3,4) & -\mathbf{U}_1(3,5) & -\mathbf{U}_1(3,6) \end{bmatrix}. \tag{A.3}$$

The expressions for $\mathbf{T}_1(1,1)$, $\mathbf{T}_1(1,2)$, etc. and $\mathbf{U}_1(1,1)$, $\mathbf{U}_1(1,2)$, etc. are given in pp. 701–703 of Ref. [9].

References

[1] C.G. Lai, A. Callerio, E. Faccioli, V. Morelli, P. Romani, Prediction of railway-induced ground vibrations in tunnels, *Journal of Vibration and Acoustics, Transactions of the ASME* 127 (5) (2005) 503–514.

[2] X. Sheng, C.J.C. Jones, D.J. Thompson, Ground vibration generated by a harmonic load moving in a circular tunnel in a layered ground, in: *Proceedings of the 10th International Meeting on Low Frequency Noise and Vibration and Its Control*, 2002, pp. 161–176.

[3] X. Sheng, C.J.C. Jones, D.J. Thompson, Prediction of ground vibration from trains using the wavenumber finite and boundary element methods, *Journal of Sound and Vibration* 293 (3–5) (2006) 575–586.

[4] D. Clouteau, M. Arnst, T.M. Al-Hussaini, G. Degrande, Freefield vibrations due to dynamic loading on a tunnel embedded in a stratified medium, *Journal of Sound and Vibration* 283 (1–2) (2005) 173–199.

[5] G. Degrande, D. Clouteau, R. Othman, M. Arnst, H. Chebli, R. Klein, P. Chatterjee, B. Janssens, A numerical model for ground-borne vibrations from underground railway traffic based on a periodic finite element–boundary element formulation, *Journal of Sound and Vibration* 193 (3–5) (2006) 645–666.

[6] L. Andersen, C.J.C. Jones, Vibration from a railway tunnel predicted by coupled finite element and boundary element analysis in two and three dimensions, in: *Proceedings of the Fourth International Conference on Structural Dynamics—EURODYN2002*, Munich, Germany, 2002, pp. 1131–1136.

[7] L. Andersen, C.J.C. Jones, Coupled boundary and finite element analysis of vibration from railway tunnels—a comparison of two- and three-dimensional models, *Journal of Sound and Vibration* 293 (3–5) (2006) 611–625.
[8] R.M. Thornely-Taylor, The prediction of vibration, ground-borne and structure-radiated noise from railways using finite difference method—Part 1—theory, *Proceeding of the Institute of Acoustics* 26 (2) (2004) 69–79.
[9] J.A. Forrest, H.E.M. Hunt, A three-dimensional model for calculation of train-induced ground vibration, *Journal of Sound and Vibration* 294 (4–5) (2006) 678–705.
[10] J.A. Forrest, H.E.M. Hunt, Ground vibration generated by trains in underground tunnels, *Journal of Sound and Vibration* 294 (4–5) (2006) 706–736.
[11] S. Gupta, M.F.M. Hussein, G. Degrande, H.E.M. Hunt, D. Clouteau, A comparison of two numerical models for the prediction of vibrations from underground railway traffic, *Soil Dynamics and Earthquake Engineering* 27 (7) (2007) 608–624.
[12] M.F.M. Hussein, H.E.M. Hunt, The PiP model, a software application for calculating vibration from underground railways, in: *Proceedings of the 14th International Congress of Sound and Vibration*, Cairns, Australia, July 2007.
[13] The PiP model 2006 〈http://www.pipmodel.com〉.
[14] M.F.M. Hussein, H.E.M. Hunt, A power flow method for evaluating vibration from underground railways, *Journal of Sound and Vibration* 293 (3–5) (2006) 667–679.
[15] M.F.M. Hussein, S. Gupta, H.E.M. Hunt, G. Degrande, J.P. Talbot, A computationally efficient model for calculating vibration from a railway tunnel embedded in a half-space, *The International Journal for Numerical methods in Engineering*, in press.
[16] H. Grundmann, K. Muller, Dynamic interaction of a plate elastically mounted on a tunnel, in: Proceedings of the Sixth European Conference on Structural Dynamics, EURODYN, Paris, France, 2005, pp. 1273–1278.
[17] V.A. Babeshko, M.G. Seleznev, T.N. Selezneva, V.P. Sokolov, On a method of studying steady-state oscillations of an elastic half-space containing a cavity, *Applied Mathematics and Mechanics (English translation of Prikladnaya Matematika i Mekhanika)* 47 (1) (1983) 88–93.
[18] G.E. Kolodyazhnaya, M.G. Seleznev, T.N. Selezneva, Problem of a uniformly moving oscillating load acting on an elastic half-space containing a recessed cylindrical cavity, *Mechanics of Solids (English translation of Izvestiya Akademii Nauk SSSR, Mekhanika Tverdogo Tela)* 22 (6) (1987) 83–87.
[19] M.F.M. Hussein, H.E.M. Hunt, Modelling of floating-slab tracks with continuous slabs under oscillating-moving loads, *Journal of Sound and Vibration* 297 (1-2) (2006) 37–54.
[20] K.F. Riley, M.P. Hobson, S.J. Bence, *Mathematical Methods for Physics and Engineering*, Cambridge University Press, Cambridge, 2000.
[21] M. Shamalta, A.V. Metrikine, Analytical modelling of the dynamic response of an embedded railway track to a moving load, *Archive of Applied Mechanics* 73 (1–2) (2003) 131–146.
[22] H.A. Dieterman, A.V. Metrikine, Critical velocities of a harmonic load moving uniformly along an elastic layer, *Journal of Applied Mechanics, Transactions of the ASME* 64 (1997) 596–600.
[23] G. Strang, *Linear Algebra and Its Application, third edition*, Harcourt Brace Jovanovich College Publishers, 1988.
[24] Matlab 6.5.0.18091 3a, Release 13, The Mathworks Inc., 2002.
[25] K.F. Graff, *Wave Motion in Elastic Solids*, Oxford University Press, London, 1975.
[26] D.C. Gazis, Exact analysis of the plane–strain vibrations of thick-walled hollow cylinders, *Journal of the Acoustical Society of America* 30 (8) (1958) 786–794.
[27] D.C. Gazis, Three-dimensional investigation of the propagation of waves in hollow circular cylinders. I. Analytical foundation, *Journal of the Acoustical Society of America* 31 (5) (1959) 568–573.
[28] D.C. Gazis, Three-dimensional investigation of the propagation of waves in hollow circular cylinders. II. Numerical results, *Journal of the Acoustical Society of America* 31 (5) (1959) 573–578.
[29] S. Stearns, *Digital Signal Analysis*, Hayden Book Company Inc., New Jersey, 1983.
[30] W.H. Press, B.P. Flannery, S.A. Teukolsky, W.T. Vetterling, *Numerical Recipes in Pascal*, Cambridge University Press, Cambridge, 1998.
[31] D. Zeitlin, On several applications of the first derivative of a determinant (in Mathematical Notes), *American Mathematical Monthly* 70 (1) (1963) 58–60.
[32] A. Bostrom, A. Burden, Propagation of elastic surface waves along a cylindrical cavity and their excitation by a point force, *Journal of the Acoustical Society of America* 72 (3) (1982) 998–1004.
[33] J.W. Rayleigh, *The Theory of Sound*, vol. 1, Dover, New York, 1894 Reprint 1945.
[34] T.D. Rossing, N.H. Fletcher, *Principles of Vibration and Sound*, Springer, New York, 1994.
[35] J.J. Azar, *Matrix Structural Analysis*, Pergamon Press Inc., Oxford, 1972.